RI 9169

Bureau of Mines Report of Investigations/1988

Coal Particle Pyrolysis Mechanisms and Temperatures

By Martin Hertzberg, Isaac A. Zlochower, and John C. Edwards

UNITED STATES DEPARTMENT OF THE INTERIOR

Report of Investigations 9169

Coal Particle Pyrolysis Mechanisms and Temperatures

By Martin Hertzberg, Isaac A. Zlochower, and John C. Edwards

UNITED STATES DEPARTMENT OF THE INTERIOR
Donald Paul Hodel, Secretary

BUREAU OF MINES
T S Ary, Director

Library of Congress Cataloging-in-Publication Data

Hertzberg, Martin
Coal particle pyrolysis mechanisms and temperatures.

(Report of investigations ; 9169)

Bibliography: p. 35-36.

Supt. of Docs. no.: I 28.23:9169.

1. Coal—Combustion. 2. Pyrolysis. 3. Chemical reaction, rate of. I. Zlochower, Isaac A. II. Edwards, John C. III. Title. IV. Series: Report of investigations (United States. Bureau of Mines) ; 9169.

TN23.U43 [TP325] 622 s [621.402'3] 87-600350

CONTENTS

ILLUSTRATIONS

TABLES

UNIT OF MEASURE ABBREVIATIONS USED IN THIS REPORT

atm	atmosphere	kJ/cm^3	kilojoule per cubic centimeter
BTU/lb	British thermal unit per pound	μm	micrometer
°C	degree Celsius	$\mu m/s$	micrometer per second
cal cm^{-2}	calorie per square centimeter	mg/cal	milligram per calorie
$cal/(cm^2 \cdot s)$	calorie per square centimeter second	$mg/(cm^2 \cdot s)$	milligram per square centimeter second
cal/(cm·s·°C)	calorie per centimeter second degree Celsius	mg/J	milligram per joule
cal/g	calorie per gram	min	minute
cal/(g·°C)	calorie per gram degree Celsius	mm	millimeter
cal/(g·K)	calorie per gram Kelvin	ms	millisecond
cm	centimeter	mW/(cm·K)	milliwatt per centimeter Kelvin
cm/s	centimeter per second	pct	percent
g/cm^3	gram per cubic centimeter	s	second
g/kcal	gram per kilocalorie	s^{-1}	reciprocal second
J/(g·°C)	joule per gram degree Celsius	W/cm^2	watt per square centimeter
K	kelvin	yr	year

COAL PARTICLE PYROLYSIS MECHANISMS AND TEMPERATURES

By Martin Hertzberg,[1] Isaac A. Zlochower,[2] and John C. Edwards[3]

ABSTRACT

This Bureau of Mines report analyzes diverse observations of the rates and mechanisms for the pyrolysis and devolatilization of coal and polymethylmethacrylate (PMMA). New data are presented for PMMA, together with new morphological evidence for the microscopic structure of the pyrolysis and devolatilization wave front in coals. It is concluded that there is no substantive evidence to support the traditional viewpoint that the pyrolysis and devolatilization rate process occurs isothermally, under chemical rate control; or is described realistically by a classical, unimolecular Arrhenius function of temperature. Instead, the reaction process occurs as a highly nonisothermal, heat-flux-driven, pyrolysis and devolatilization wave front, whose speed of propagation is predictable by internal heat transport constraints.

Except for the complication of its char-layer residue, whose increasing thickness insulates the pyrolysis wave front from the heat source flux that drives it, both coal and PMMA behave similarly during pyrolysis and devolatilization. For PMMA, decomposition occurs at a temperature of 350° to 550° C; for coal it occurs at 450° to 600° C. There is no evidence that the reactant temperature ever exceeds those values regardless of the source temperature to which the samples are exposed.

[1] Supervisory research chemist.
[2] Physical scientist.
[3] Research physicist.
Pittsburgh Research Center, Bureau of Mines, Pittsburgh, PA.

INTRODUCTION

An accurate description of the coal pyrolysis and devolatilization process is essential for a thorough understanding of coal technology in all of its stages: from the mining of coal to its end uses in industrial furnaces, high-intensity combustors, or utility boilers. Coal mining operations involve serious safety hazards associated with combustion processes that occur accidentally in the form of unwanted coal fires and dreaded coal dust explosions. Such fires and explosions proceed via a complex sequence of processes (a mechanism) whose first step is the thermal pyrolysis and devolatilization of coal (*1*)[4] or coal dust (*2–3*). Similar fire and explosion hazards are present during the transportation of coal, its handling and storage, its cleaning and drying, and in the pulverization and burning of coal in kilns, industrial furnaces, or electric power generating stations (*4–6*).

The volatile yield of a coal, and its onset temperature for pyrolysis, determines the minimum autoignition temperature of a coal dust cloud (*7*). The minimum autoignition temperature determines its ease of thermal ignition. The ease of ignition plays a role in the safe utilization of coals. The volatile yield and the onset temperature for pyrolysis are determined by the chemical structure of the coal and the detailed mechanism by which that structure transforms into volatiles during the process of thermal pyrolysis (*8*). The rate of devolatilization and the yield of volatiles are of major importance in the technology of coal utilization: in the design of stable and efficient burners and in the control of pollutants generated by combustion. The devolatilization mechanism determines the nature and structure of the char residue, whose surface area determines its burnout rate and the carbon burnup efficiency of utility boilers. And finally, the devolatilization process is the critical first step in the gasification or liquification of coal. Accordingly, the development of a cost-effective synthetic fuels industry based on coal requires a thorough understanding of that same pyrolysis and devolatilization process.

At the present time, the understanding of the pyrolysis and the devolatilization process appears in the form of two predominant theories, or models: One is the traditional viewpoint that the process is under chemical reaction rate control (*9–10*); the other is a more recent viewpoint that the process is under internal thermodynamic heat transport control (*11–12*). This report will first contrast those different points of view in terms of their underlying assumptions. It will then proceed to summarize the available evidence, both experimental and theoretical, which supports the newer theory of heat transport control.

The evidence to be summarized is multifaceted. It includes devolatilization rate data for coal obtained both as a function of particle size and source flux intensity. These data are supplemented by direct microscopic evidence of the structural or morphological changes that occur during the devolatilization process. Also included is earlier Bureau data on the temperature structure of coal during its pyrolysis at low fluxes (*1*), as well as indirect information on the thermal structure that can be inferred from the above morphological records. These considerations are also related to the problem of making direct, optical temperature measurements of the reacting coal during the course of its active pyrolysis and devolatilization, and how such measurements are complicated by the presence of the char-layer residue.

The new viewpoint of thermodynamic transport control is also be applied to another pyrolyzing solid, polymethylmethacrylate (PMMA) (*13*), for which the complication of a char-layer residue is absent. The initial presentation of the new theory of heat transport control is in the form of a quasi-steady-state theory. This report concludes with a more formal development of the theory in a general form and a non-steady-state development based on the time-dependent conservation equation. The predictions of the time dependent theory are also compared to the data.

THE TRADITIONAL MECHANISM—CHEMICAL KINETIC RATE CONTROL

For the traditional mechanism in its simplest form, the pyrolysis and devolatilization reaction

$$\text{Coal} \rightarrow \text{Volatiles} + \text{Char} \qquad (1)$$

is treated as a first-order or unimolecular reaction. The reaction is assumed to be under chemical kinetic rate control and to proceed uniformly throughout the isothermal mass of coal at a temperature, T. For a unimolecular reaction, the rate is proportioned to the concentration of the reactant. For a pure substance that decomposes completely into volatile products, the reaction rate is proportional to its rate of weight loss, $-\,d\,m(t)/dt$. The concentration of reactant is given by its mass m(t) and the unimolecular rate law is expressed as $-\,d\,m(t)/dt = k\,m(t)$. For coal, the decomposition is not complete since there is always a char residue left whose final mass is $m(\infty)$, even after the reaction goes to completion. In that case, the concentration of reactant is given by the mass of unreacted coal that is capable of generating volatiles, which is $m(t) - m(\infty)$. The reaction rate is measured by the rate of loss of that unreacted mass, which is given by $-\,d/dt\,[m(t) - m(\infty)] = -\,d\,m(t)/dt$. Thus for the traditional, unimolecular decomposition mechanism represented by equation 1, one obtains

$$-\,d\,m(t)/dt = k\,[m(t) - m(\infty)], \qquad (2)$$

where m(t) is the sample mass at any time, t, and $m(\infty)$ is the final mass of the completely devolatilized sample; i.e., the mass of the char residue at $t = \infty$.

The mass difference, $m(t) - m(\infty)$, is the mass of the reactant: the mass of coal that is still capable of being

[4] Italic numbers in parentheses refer to items in the list of references preceding the appendixes.

devolatilized at any time, t. Initially at t = 0, before its exposure at some elevated decomposition temperature, m(t) = m_o, where m_o is the initial mass of coal. Initially all of the potential volatiles, $m_o - m(\infty)$, are contained within the solid coal mass and are available for reaction. As the reaction proceeds, the mass of the sample decreases from m_o to m(t), as pyrolysis occurs and volatiles evolve from the sample and are lost. The reaction is complete at t = ∞, when m(t) = m(∞) and all the volatiles have been removed. Only the char residue of mass, m(∞), is then left.

Equation 2 may be rewritten in the form

$$d\,V(t)/dt = k[V(\infty) - V(t)], \quad (3)$$

where V(t) is the volatile yield, in percent, after an exposure time, t, and V(∞) is the maximum volatile yield as t $\rightarrow \infty$. The pyrolysis and devolatilization mass loss experiments are done in an inert atmosphere so that there is no oxidation weight loss of the char. The weight loss measured after each exposure time, t, is then only that associated with the pyrolysis and devolatilization process. For such experiments, $V(t) = 100\,[m_o - m(t)]/m_o$.

For a unimolecular reaction, the rate constant, k, in equation 3 is traditionally given by the classical, Arrhenius exponential function

$$k = k_o\, e^{-E_a/RT}, \quad (4)$$

where k_o is a preexponential factor, E_a is the activation energy, R is the universal gas constant, and T is the exposure temperature in degrees absolute.

The data obtained by most of the early reseachers for the pyrolysis and devolatilization of coal subjected to elevated temperatures by a variety of heating methods, were generally analyzed by this traditional mechanism (*9–10*). Even the more recent researchers using more elaborate methods of controlling heating rates and exposure times tend to analyze their data in terms of this traditional mechanism or by derivatives of the mechanism which involve more complex kinetic pathways (*10, 14*). A summary of much of the early data analyzed in those terms has been given by Howard (*10*). The data reveal a wide variation in the absolute rate constants and activation energies among the various investigators using various methods of high-temperature exposure.

It has long been recognized that the simple, unimolecular kinetic model represented by equations 3 and 4 is, at best, only a crude approximation. The major efforts in correcting the analysis have, however, focused mainly on correcting the oversimplification associated with the use of a one-step reaction rate scheme (equation 1). Almost no effort has gone into challenging the fundamental assumption that the process is controlled by chemical kinetic reaction rates. Thus, for example, Chermin and Van Krevelen (*15*), proposed a pyrolysis model based on three consecutive unimolecular reactions:

Coal → Metaplasts,
Metaplasts → Semicoke + Primary Volatiles,
Semicoke → Char (coke) + Secondary Volatiles.

The model was applied to the plasticity behavior of coking coals in bulk form undergoing pyrolysis and devolatilization.

A major problem with either the earlier one-step kinetic scheme, or the preceding three-step model, is their inconsistency with the data obtained for relatively small particles at high heating rates or exposure temperatures. For example, the measured V(∞) values are not entirely constant but depend on both exposure temperature and temperature history or heating rate. The measured V(∞) values at high exposure temperatures, high heating rates, and for small particle sizes, can be as much as a factor of 2 higher than their values obtained at lower temperatures, lower heating rates, and larger particle sizes (*10*). In addition, the rate constant, k, depends not just on the exposure temperature, T, but also on the heating rate, dT/dt, or the temperature history.

Such hysteresis effects were considered by Juntgen and van Heek (*16*). Their model maintained the unimolecular Arrhenius kinetic function and simply introduced an *ad hoc* dependence on heating rate in an explicit way. Howard (*10*) has reviewed the various modifications to the kinetic rate models that have been proposed by researchers over the years. He also developed a model based on a large number of parallel reactions, one for each product specie generated by the pyrolysis reaction, and used a statistical distribution of activation energies.

Over the years, considerable effort has gone into the development of a variety of such chemical rate control models; however, very little effort has been devoted to a thorough analysis of the heat transport processes by which the particles are elevated to pyrolysis temperatures when they are first brought into contact with the high-temperature source. It was generally assumed, especially by the earlier researchers, that the temperature of the exposed coal particles would rapidly reach the high temperature of the furnace walls, or the hot gases, or the electrically heated metal screens to which they were exposed.

Recent research attempted to justify that assumption by an occasional analysis of the heat transport problem (*17*); however, those analyses were either unrealistic or they were simply ignored because they involved too much uncertainty. A major exception can be found in the analyses of Zielinski (*18*), but his conclusions have generally been ignored. He analyzed the devolatilization rate data reported by many different investigators who had used a variety of heating sources to study coal particles of varying sizes from as small as 20 μm in diameter to as large as 3,000 μm (3 mm). Zielinski concluded that the rate of heat transfer from the heating source to the coal particle exerted the dominant influence in determining the rate of evolution of volatiles. The previously observed dependence on heating rate was thus explained in terms of a heat transport limitation from the heating source *to* the particle. He cautioned against the "danger that in describing the so-called high temperature process, the temperature assigned to the coal will be estimated incorrectly, and may be [incorrectly taken as] the temperature of the heat carrier or the container walls and not that of the coal particles themselves." He noted that measurements of the temperature of the coal particles themselves were "very rare indeed." Unfortunately, that situation had not significantly changed in the 20 yr since Zielinski's analysis, with only one possible exception (*19*).

If indeed, as Zielinski had suggested, the particle temperatures are grossly overestimated by assuming that they instantaneously reach the source temperature, then the inferred rate constants are grossly underestimated. Furthermore, the use of more complex kinetic schemes to account for apparent heating rate effects that may not be real but are only reflections of heat transport limitations, can only serve to confuse the issue. In view of the gross

overestimation of particle temperatures by previous researchers, Zielinski was justifiably skeptical of their measured, apparent activation energies since they were much lower than the known values for the bond energies of the coal structural bonds that are broken during pyrolysis. If real particle temperatures were lower than those assumed because of heat transport limitations to the particles, then the real activation energies should be correspondingly higher than those calculated by ignoring those heat transfer limitations. Detailed calculations reported by Friehaut and Vastola (*20*) show that those apparent activation energies would be much lower than their true values. If properly corrected, those activation energies can become realistic in relation to the known bond energies.

Zielinski's arguments (*18*) are strongly reinforced by Freihaut and Vastola's (*20*) calculations, by Solomon's recent reanalysis of the particle pyrolysis data (*21*), and by the particle temperature measurements reported by Solomon (*19*). Solomon notes that at a given exposure temperature (800° C), the unimolecular devolatilization rate constants reported in the literature vary by as much as two orders of magnitude: from as low as 1 s^{-1} to as high as 100 s^{-1}. Since particle temperatures were not directly measured but were usually assumed to be equal to the source temperature, he argues that the causes of the discrepancies are the inaccurate estimates of particle temperatures by the various researchers. For spherical particles that heat up isothermally during their omnidirectional exposure to a hot gas source at temperatures, T_h, in a furnace of unit emissivity whose walls are at that same source temperature, the rate of increase of particle temperature is given by

$$V_p\, C(T)\, \rho \frac{dT}{dt} = \frac{Nu\, \lambda\, (T_h - T)}{D_p} A_p + \epsilon_p\, \sigma\, (T_h^4 - T^4)\, A_p. \quad (5)$$

The particle temperature, T, is a function of time, t. The particle is assumed to heat up isothermally, and that assumption is equivalent to the assumption that it has an infinitely high thermal conductivity. That unrealistic assumption will be corrected in the analysis to be presented in the following section; however, for purposes of understanding the problem of heat transport limitations *to* the particle, the assumption of infinite thermal conductivity will be made as a first approximation. The particle volume is V_p, its surface area is A_p, and its diameter is D_p. The particle density is ρ and C(T) is the heat capacity of the particle. The quantity Nu is the Nusselt number for heat transfer from the hot gas to the cold particle; and λ is the thermal conductivity of the boundary layer through which heat is transported from the hot gas source to the particle. The particle has an emissivity, ϵ_p, which is equal to absorptivity; and σ is the Stefan-Boltzmann constant. Solving equation 5 for the rate of temperature rise as a function of particle diameter gives

$$\frac{dT}{dt} = \frac{6}{\rho\, C(T)} \frac{Nu\, \lambda\, (T_h - T)}{D_p^2} + \frac{\epsilon_p \sigma\, (T_h 4 - T^4)}{D_p}. \quad (6)$$

In previous analyses of this problem, the emissivity was generally taken to be unity and the heat capacity was usually taken as the room temperature value. Solomon (*21*) has reanalyzed the problem and concluded that a much higher heat capacity value is required as the particle temperature increases (*21*). Merrick's review (*22*) of the heat capacity data for coal indicates that the heat capacity at 800° C is about a factor of 2.5 higher than its room temperature value. In addition, a much lower absorptivity (ϵ_p) should be used based on the recent optical measurements of Solomon (*23*). If both of those correction factors are used, they result in a lower rate of increase in particle temperature than was previously assumed.

Accordingly, the corrected particle temperatures obtained by Solomon are considerably lower than the values previously used. They are, in fact, substantially lower than the source temperatures during the entire course of the devolatilization process. The rates previously reported were assumed to have been measured at the source temperature, T_h. In reality, however, they were measured at a much lower particle temperature, T. Solomon's corrected rate constants (*19, 21*) at a given temperature are accordingly higher than those of the previous investigators and his corrected activation energies are also higher. His corrections also reduce the discrepancies in the reported rates and narrow the range of their variations. Solomon's resolution of the problem is thus entirely consistent with Zielinski's earlier analysis of the heating rate dependencies and his conclusion that the published data were dominated by heat transport limitations from the heating source to the particles.

Further support for those arguments come from the direct optical measurements of particle temperatures during pyrolysis that were reported by Serio, Solomon, Hamblen, Markham, and Corangelo (*19*). For coal particles in an entrained flow reactor whose source temperature, T_h, was 1,300° C, coal particles with sizes between 45 and 75 μm were completely devolatilized by the time they reached particle temperatures, T, of 700° to 800° C. In the absence of a direct measurement of those temperatures, previous investigators would have simply assigned the measured devolatilization rate in that experiment to the source temperature, 1,300° C. In reality, the measured rate should apply to a temperature range that is probably lower than 700° C.

In addition, for such omnidirectional heating of coal, there is always a char residue that remains on the outside of the particle after pyrolysis. If the particle is not isothermal, there is inevitably a hotter char layer on the surface which can conceal a lower temperature region of coal pyrolysis below. The optical particle temperature measurements will inevitably include a dominant contribution from the higher temperature char residue. Thus, there is still some uncertainty as to whether even those *measured* particle temperatures should be assigned to the devolatilizing coal or to the hotter surface char residue that was formed by the devolatilization process that had previously occurred at an even lower temperature.

Thus, even those direct temperature measurements may not go far enough in correcting the devolatilization rate data. There are, in fact, other reasons for suggesting even larger correction factors and higher rates than those previously reported using the traditional mechanism, and the traditional treatment of the data which ascribes the source temperature, T_h, to the particle temperature, T. While the above analysis of heat transport limitations is reasonable as far as it has gone, it still has not gone far enough in evaluating all the heat transport limitations. At least three additional correction factors are required.

First, equations 5 and 6 are reasonably valid for particles only while they are essentially inert; that is, only before they begin to pyrolyze and devolatilize. Once the

particles begin to react and to generate volatiles, the outward flow of gaseous pyrolysis products will markedly reduce the conductive heat transport flux from the hot gas to the particle. Pyrolysis gases are emitted at the onset temperature for devolatilization (~450° C) and they are much colder than the surrounding gases, which are at the source temperature, T_h. The effect is sometimes referred to as the blowing effect: a convective, outward flow of cooler gas that shields the particle from the hot surroundings, and counteracts the conductive heat flow inward. For small, *inert* particles, Nu ~ 2 because the boundary layer thickness for conduction from the source gas at T_h, to the particle at T, is comparable in dimensions to the particle diameter, D_p. But the colder, outward-flowing volatiles emitted from the particles are gases that are much less dense than the coal particle from which they were generated, and accordingly, they dilute and cool the hot gas surroundings. In effect, that dilution and cooling transports the hot boundary to a distance that is much larger than D_p. This blowing effect increases the boundary layer thickness which reduces Nu and the corresponding temperature gradient that is conducting heat to the particle. The effective thermal conductivity, λ, is also reduced by the cooling, outward flow of transpiring volatiles. There is thus a marked reduction in dT/dt as soon as anything happens, and the particle begins to pyrolyze and devolatilize.

Secondly, as the particle begins to react, the heat flux passing into its surface from the hot surrounding gas is no longer exclusively available to raise the particle temperature. An additional term, $\frac{dm(t)}{dt}\Delta H_v$ must be added to the left-hand side of equation 5. Since the pyrolysis and devolatilization process involves the rupture of strong bonds in the polymeric structure of coal, the heat flux being absorbed by the particle must also supply the endothermic heat of devolatilization, ΔH_v. Thus, in addition to the heat capacity integral $\int_{T_o}^{T} C(T)\,dT$ which represented the particle's thermal inertia or resistance to an increase of temperature while the particle was still inert, once it begins to react an additional thermal inertia or resistance appears in the form of the heat of devolatilization. Thus an even higher effective heat capacity correction is required once the particle begins to devolatilize significantly, and that endothermic reaction process drastically limits the rate of particle temperature rise in the presence of a given heat flux passing through its surface. This factor will be considered more quantitatively in the next section.

The third correction factor required will also be considered in depth in the next section. It has already been alluded to in discussing the char-layer complication for coal and its effect on particle temperature measurements. The analysis, thus far, has been limited to the problem of heat transport limitations *to* the particle from the heat source. There is an equally important problem that deals with the question of heat transport limitations *within* the particle; that is *through* the particle, from its surface to its interior. If a particle were actually isothermal, as is assumed even by Solomon, then according to the second law of thermodynamics no heat could be transported from its surface to its interior. Where then, would the heat flux come from to overcome the thermal inertia of the reacting mass in the interior of the particle?

Clearly, even though he has attempted to correct for the heat transport limitations *to* the particle, Solomon has not considered the problem of the thermal structure *within* the particle. He still assumes that the particle reacts isothermally and that the process is under chemical kinetic rate control at the corrected particle temperature. As has been pointed out by Hertzberg (2), this traditional mechanism of an isothermal reaction occurring uniformly throughout the particle under chemical-kinetic rate control, provides an unreal physical picture of the process. The traditional mechanism implies that the particle pyrolyzes and devolatilizes simultaneously everywhere throughout its volume without first experiencing a thermal heating or decomposition wave, and without the normal limitations on the transport of heat and mass from one region of the particle to another. Such behavior is physically impossible even on the microscopic scale. It is as physically impossible as the instantaneous action at a distance assumption that underlies the traditional or classical mechanics of Newton or the classical electrodynamics of Coulomb's law.

As shown by Maxwell and Einstein, changes in the distribution of electric charges or mass in one region of space do not instantaneously influence the electromagnetic or gravitational fields throughout the universe: The effects of those changes are propagated at a finite velocity, c. Similarly, heat and mass are not instantaneously transmitted from one region of a coal particle to another at an infinite speed: They are limited to propagation at a finite rate. If the source of heat is outside of the particle, its surface must pyrolyze first before the interior of the particle can react, and volatiles generated in the interior of the particle cannot instantaneously dematerialize: They must transport themselves to the surface at a finite rate, and be emitted from the surface before their weight loss can be registered.

This final correction factor involves such internal transport limitations, and the attempt to address those limitations leads, naturally, to a proposed new mechanism, or theory for the pyrolysis and devolatilization of coal.

THE NEW MECHANISM—INTERNAL HEAT TRANSPORT CONTROL

In its simplest form, the theory is a manifestation of the first law of thermodynamics. One considers a planar solid surface that is pyrolyzing and devolatilizing in a steady-state condition as it is being subjected to a radiant heat source flux intensity, I. The system for coal is depicted in figure 1. The coal case is more complicated than necessary because of the existence of the residual char layer. For the moment, the existence of that char layer will be ignored, and it will be assumed that the substance devolatilizes completely so that the incident flux is directly absorbed at the devolatilizing surface. The temperature of that surface is assumed to be at some discrete

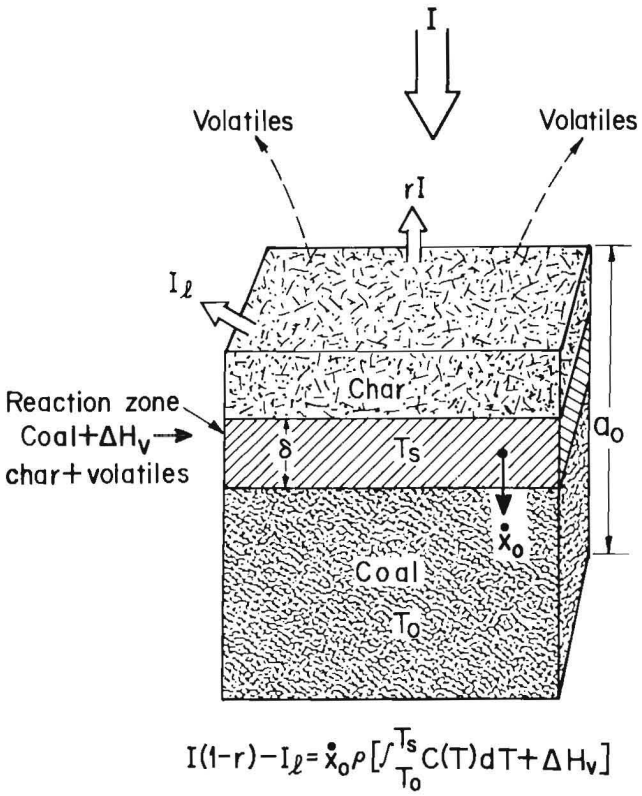

Figure 1.—Schematic idealization of propagation of a planar, steady-state pyrolysis and devolatilization wave front in coal as it is being driven by a plane-wave radiant source flux of intensity, I.

decomposition temperature, T_s. Examples of such non-char-forming substances are polymeric solids that pyrolyze and devolatilize completely, such as polymethylmethacrylate (PMMA), for example (*13*), or even more ideally, inorganic solids that sublime directly into vapors of known composition.

For simplicity, it is assumed that the incident heat source flux is radiative, from a laser beam that is normal to the planar surface. The radiative flux from the laser is assumed to be absorbed at the devolatilizing surface. There is a fraction of the incident flux that is reflected, rI, and another fraction that is lost to the surroundings, I_ℓ. The net loss flux, I_ℓ, is the sum of several loss components: the heat lost by conduction and convection to the surroundings, plus that lost by reradiation from the heated regions of the devolatilizing solid. For the steady-state regression or propagation of the devolatilization wave at the linear rate, $\dot{x}_o$, the first law of thermodynamics requires that the net absorbed flux, $I(1-r)$-I_ℓ, supply the power necessary to first, bring each volume element of the solid with its heat capacity, C(T) to its decomposition temperature, T_s, and secondly supply the heat of devolatilization, ΔH_v. Thus

$$I(1 - r) - I_\ell = \dot{x}_o\rho \left[\int_{T_o}^{T_s} C(T)dT + \Delta H_v\right]. \qquad (7)$$

For a cubic particle with edge lengths, a_o, the time required for its complete devolatilization is simply the time required for the devolatilization wave to traverse completely through the particle. Thus

$$t_{dv} = \frac{a_o}{\dot{x}_o} = \frac{a_o\rho\left[\int_{T_o}^{T_s} C(T)dT + \Delta H_v\right]}{[I(1-r) - I_\ell]} = \frac{\alpha D_p}{I(1-r) - I_\ell} \cdot \qquad (8)$$

The first law of thermodynamics, equation 8, thus predicts that the particle devolatilization time should vary linearly with the particle diameter, and inversely with the *absorbed* flux. It is assumed in equation 8 that the cubic particle is oriented so that one of its faces is perpendicular to the laser beam, as depicted figure 1. If the particle is spherical, or if the orientation with respect to the beam is random, then a geometric correction factor is required in order to relate a_o to the spherical particle diameter, D_p. That factor is included in the constant, α.

For a spherical particle that is heated by conduction only from a hot gas source, $I = Nu\,\lambda\,(T_h - T)/D_p$, and one obtains:

$$t_{dv} = \frac{\alpha D_p 2}{Nu\,\lambda\,(T_h - T)} = \beta D_p^{\,2}, \qquad (9)$$

in the limit as $I_\ell << I$. For purely conductive heating, the devolatilization time should vary as the square of the particle diameter; however, that prediction assumes that I_ℓ, Nu, and λ are insensitive to particle diameter. As indicated earlier, the blowing effect of volatiles convecting from the reacting particle can alter the magnitude of those quantities and may complicate the preceding prediction if those quantities display their own D_p dependence during the course of the devolatilization process. For those reasons, the laser or radiant source heating method is cleaner than the hot gas source method of heating. The input heating flux, I, is directly controllable and can be maintained constant during the course of the experiment quite independently of the dynamics of the devolatilization process. For the hot gas source, the net input flux is coupled to the devolatilization dynamics, and its magnitude is not therefore directly controlled by the investigator.

An early use of the laser pyrolysis method goes back to the decade when the high-power, infrared CO_2 laser was first invented. That laser was used to study the burning rate of pure ammonium perchlorate (NH_4ClO_4), which is used as the oxidizing component in solid rocket propellants. Although pure NH_4ClO_4 is a monopropellant, it does not normally sustain a self-deflagration wave by itself at atmospheric pressure. It takes about 20 atm for it to burn freely, which makes experimentation with the pure solid somewhat inconvenient. But in a laser beam, above a certain threshold flux, the deflagration wave is sustained at atmospheric pressure (*24–25*).

The earliest experiments reported by Hertzberg (*24–25*) and later by Pellett (*26*) provided a convenient test of equation 7. The measured regression rate, $\dot{x}_o$ (NH_4ClO_4), was linearly proportioned to the incident flux above a certain loss threshold, I_ℓ. Furthermore, its absolute magnitude was predicted reasonably well by the thermodynamic heat transport constraints of equation 7. The reaction rate of the devolatilization process was thus directly predictable from the first law of thermodynamics without any additional assumptions regarding the chemical kinetics of the process. Those experiments provided an early test of the validity of the new mechanism.

RATE DATA

LARGE (MACROSCOPIC) COAL SAMPLES

In terms of their detailed spatial resolution, the best data available for coal pyrolysis and devolatilization were reported by Lee, Singer, and Chaiken (*1*). Their data were obtained with an infrared (10.6-μm) CO_2 laser source at fire-level heat fluxes of from 3 to 8 W/cm^2 [0.76 to 2.0 cal/(cm^2·s]. Their "particles" were large, solid coal cylinders, 1.8 cm in diameter and 5 cm high. The cylinders were oriented so that the laser heating flux was incident on the upper face of the cylinder. The pyrolysis wave was initiated at that upper absorbing surface and propagated downward parallel to the axis of the cylinder. Their data are reproduced in figures 2 through 5. Their mass loss fluxes as a function of exposure time for three laser flux levels are shown in figure 2. Their peak mass loss fluxes are plotted as a function of laser flux in figure 3. Their measured temperature profiles are shown in figure 4.

For their data, the bedding planes of the coal seam were oriented parallel to the axis of the cylinder, and the laser beam flux input was also parallel to that axis. Their results showed some sensitivity to the bedding plane orientation. As a whole, their data are notable because they clearly show the complexities of the heat and mass transport processes and they reveal the dominant role played by those transport limitations. The data in figures 2 through 4 show the "particle" weight loss and the "particle" temperature structure as a function of time at several incident laser flux levels. X-ray radiographs were also used to monitor the spatial distribution of the mass density within the sample as the pyrolysis and devolatilization wave progressed in time. Those data are shown in figure 5.

Their instantaneous weight loss data, at the three flux levels shown in figure 2, reveal that a finite induction time is needed in order to bring the exposed surface regions of the sample from room temperature to the temperature at which the pyrolysis process can reach some quasi-steady-state rate. The radiant energy flux absorbed near the surface is conducted into the coal cylinder, and it takes some time for a quasi-steady-state temperature profile to be established. That induction time or burn-in time is less than 1 min at an input flux level of 2 cal/(cm^2·s) and about 2 to 3 min at the lower flux levels. For a particle which is assumed to be isothermal, the rate of increase in

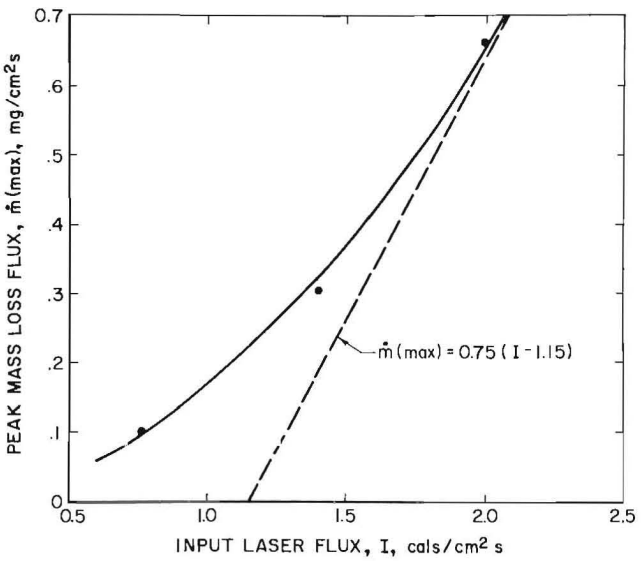

Figure 3.—Peak mass loss rates for coal as a function of source flux intensity, as measured by Lee, Singer, and Chaiken (*1*).

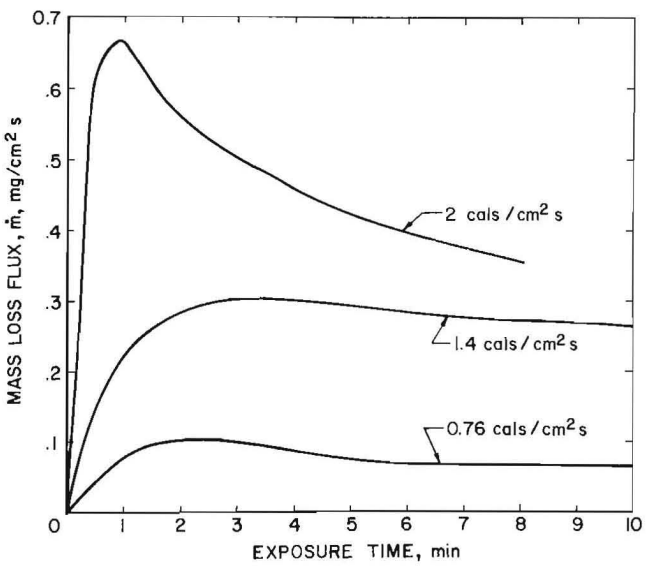

Figure 2.—Coal pyrolysis and devolatilization mass loss rates as a function of time for 1.9-cm-diameter cylinders at various laser source flux intensities, as measured by Lee, Singer, and Chaiken (*1*).

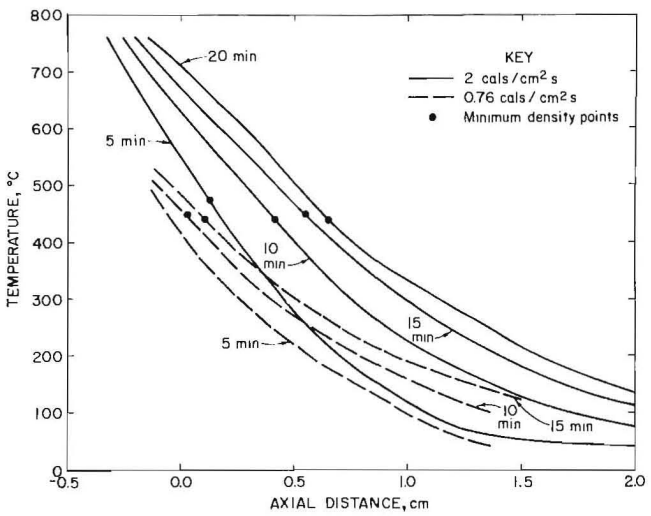

Figure 4.—Measured temperature profiles for coal during pyrolysis and devolatilization as a function of time for two laser intensities, as measured by Lee, Singer, and Chaiken (*1*).

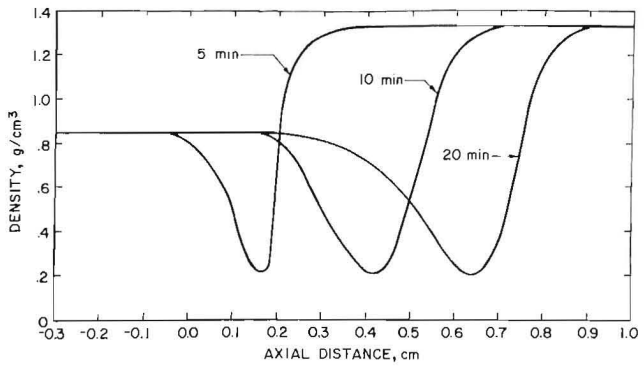

Figure 5.—Measured X-ray radiometric mass density profiles as a function of time during pyrolysis and devolatilization of coal, as determined by Lee, Singer, and Chaiken (*1*).

particle temperature is given by equation 5, which, for an input laser heating source flux, I, may be rewritten in the form

$$V_p\, C(T)\, \rho\, \frac{dT}{dt} = A_p\, [I - I_\ell'], \qquad (10)$$

where I_ℓ' is the sum of net loss flux caused by conduction-convection, reradiation, and reflection to the cold surroundings.

The cylindrical sample is, of course, not isothermal since the coal does not have an infinite thermal conductivity. In fact, coal does have fairly good thermal insulating properties, and the temperature profile that develops during pyrolysis has a finite penetration depth that is much smaller than the dimensions of the cylinder. Those penetration depths can be seen from the temperature profiles in figure 4. They are in the millimeter range during the early times and broaden as time proceeds. For a finite penetration depth, δ, the predicted induction or burn-in time becomes

$$\tau = \delta\, \rho \int_{T_o}^{T_s} C(T)dT/[I - I_\ell']. \qquad (11)$$

For the early times comparable to the induction time, $\delta \approx$ 0.2 to 0.3 cm. The heat capacity integral from ambient temperatures to their measured pyrolysis temperature of 475° C can be evaluated from the heat capacity data (*22*), and is $\int_{25°\,C}^{475°\,C} C(T)dT = \overline{C}(T)dT = 0.44\,(450) \sim 200$ cal/g. The data in figure 3 suggest that at the higher flux level of 2 cal/(cm^2·s), the loss flux I_ℓ' is about half the input flux. Setting $\rho = 1.3$ g/cm^3 and substituting into equation 11 gives $\tau = 53$ to 78 s. That calculated induction time is reasonable in comparison with the measured value of 1 min at the higher flux. At the lower fluxes of 0.76 to 1.4 cal/(cm^2·s), the τ times are correspondingly longer, and the δ depths are greater. A more exact solution for this induction time problem is presented in the "Theoretical Development" section.

Clearly the peak pyrolysis rate is attained only after an induction period, τ, as can be seen from the data in figure 2. As time proceeds, the pyrolysis wave penetrates deeper into the sample, and, as it does, it leaves a thicker char layer in its wake. That thickening char layer is depicted in figure 1, and its presence can be clearly seen from the temperature and mass density profiles shown in figures 4 and 5. The thickening char layer insulates the zone of active pyrolysis from the input laser flux. That flux is absorbed only at the uppermost surface of the char. The temperature profiles show clearly that in the presence of that insulating char layer, an additional thermal inertia must be added to equation 7;

namely $\dot{x}_o\, \rho(\text{char}) \int_{T_s}^{T_c} C(\text{char})(T)dT$, where T_c is the maximum char temperature. As the data in figure 4 show, at the highest flux the char surface temperature can approach 800° C even though the temperature of the pyrolysis wave remains fairly constant at 440° to 475° C.

As the surface temperature of the char layer increases, the reradiative losses increase markedly. For example, a char surface at 800° C with an emissivity of 0.9 reradiates a loss flux of 1.6 cal/(cm^2·s), which is about 80 pct of the incident flux, leaving a net absorbed flux of only 0.4 cal/(cm^2·s) to drive the pyrolysis wave into the remaining undevolatilized coal. Initially, during the induction period of about 1 min, that net absorbed flux was a substantially higher value of about 1 cal cm^{-2} because the losses were only about 50 pct of the incident flux.

As the char layer builds in thickness and its surface temperature increases in time, the losses increase markedly because of both reradiation and conduction-convection to the cold surroundings. As the char layer thickness increases, the surface area of contact between the hot char and the cold surroundings increases, which increases the conductive-convective loss component as well. It is not surprising, therefore, that the rate of devolatilization shown in the uppermost curve of figure 2, which is for the highest flux, decreases so dramatically after the induction time of about 1 min. The relative decrease in the rates of devolatilization for the lower flux curves are not as dramatic because their increasing loss fluxes represent a lower fraction of the incident flux. For an input flux of 0.76 cal/(cm^2·s), the temperature profiles in figure 4 show a maximum char layer temperature of only 500° C, which corresponds to a reradiating flux of 0.44 cal/(cm^2·s), which is a smaller percentage loss.

The above analysis shows clearly that the heat loss flux, I_ℓ', is a time-dependent quantity, $I_\ell'(t)$, whose value increases monotonically as the char layer builds in thickness and its surface temperature rises. Thus, although a quasi-steady-state pyrolysis wave may have been initially established after an induction time, τ, that peak rate of pyrolysis is not maintained at a constant value but decreases monotonically as the wave penetrates deeper into the cylinder because $I_\ell'(t)$ increases in time. From equation 7 one obtains

$$\dot{x}_o\, \rho = \dot{m} = \frac{I\,(1-r) - I_\ell(t)}{\int_{T_o}^{T_s} C(T)\, dT + \Delta H_v} = k_t\, [I - I_\ell'(t)], \qquad (12)$$

where k_t, the rate constant for the heat-transport-controlled pyrolysis process, is given by

$$k_t = 1/[\int_{T_o}^{T_s} C(T)dT + \Delta H_v]. \qquad (13)$$

This rate constant is simply the reciprocal of the effective heat capacity of the coal for the propagation of the pyrolysis wave through it. Clearly the coal case is considerably more complex than that of a polymeric solid that

volatilizes completely, or an inorganic solid that sublimes with no residue. For coal, there is always a char residue, and, as the pyrolysis wave penetrates deeper into the sample, an increasing fraction of the input flux, I, is lost to the surroundings as $I_\ell'(t)$. It is assumed in equation 12 that for the char layer at the coal surface, the reflectance loss, rI, is small in comparison to I, or that it can be included in the loss flux, $I_\ell'(t)$. The main losses are by conduction, convection, and reradiation to the surroundings from the char layer, and in addition, the char contributes an increasing thermal inertia to the system. As a result, the $\dot{m}$ curves decrease in time as shown in figure 2.

At the peaks of the $\dot{m}$ curves, however, a quasi-steady-state condition is nearly attained while the char layer thickness and the losses are minimal. Accordingly, equations 12 and 13 will be applied to those measured maximum values for the mass loss flux, $\dot{m}$ (max). Those measured $\dot{m}$(max) values obtained by Lee, Singer, and Chaiken are plotted in figure 3, as a function of the input flux, I. A curve is drawn through the data, and clearly there are significant nonlinearities, which suggests that $I_\ell'(t)$ (min) is not a constant fraction of I. The nonlinearity or increasing slope of the $\dot{m}$ (max) vs I curve suggests that the loss flux is not a constant absolute value, but is a fixed fraction of the incident flux. One anticipates that at the higher fluxes that will not be the case and that $I_\ell'(t)$ (min) will eventually reach some constant value. Anticipating that that condition has been reached at their highest flux, where the induction time is minimal, and where the measurements are most accurate, the best one can do with the data is to use their limiting slope at the highest flux studied. A tangent line has therefore been drawn to the curve at that point and is fitted to equation 12. The equation of that tangent line is given by $\dot{m}\,(\text{max})\,(\text{mg}/(\text{cm}^2\cdot\text{s})) = 0.75\,(\text{mg/cal})\,[I - 1.15]\,(\text{cal}/(\text{cm}^2\cdot\text{s}))$. Comparison of that tangent line slope with equation 12 gives $k_t = 0.75$ mg/cal for their measured value of the heat-transport-limited rate constant for the pyrolysis and devolatilization of Pittsburgh seam bituminous coal. By using equation 13, that rate constant corresponds to an effective heat capacity for the pyrolysis wave propagation of $\int_{T_o}^{T_s} C(T)dT + \Delta H_v = 1/k_t = 1.33 \times 10^3$ cal/g. As calculated earlier, the heat capacity integral, $\int_{T_o}^{T_s} Cp(T)dT$, is about 200 cal/g. There is probably also a significant thermal inertia correction for the presence of a char layer even at $\dot{m}$(max). That heat capacity integral $\int_{T_s}^{T_c} C(\text{char})(T)dT$ is probably of comparable magnitude to the value for the coal. Thus, this analysis with all its uncertainties, nevertheless suggests that ΔH_v is endothermic by about 900 cal/g. As will be seen later, that value grossly overestimates the heat of devolatilization.

The data of Lee, Singer, and Chaiken are here interpreted to support the mechanism of internal heat transport control. Their data indicate that the pyrolysis rate is, to a first approximation, a linear function of the absorbed flux, as predicted by equations 7 and 12. Although their coal pyrolysis rate data are complicated by the presence of a char layer, to a first approximation, their results are similar to those obtained independently by Hertzberg (*24–25*) and Pellett (*26*) for ammonium perchlorate, which is not complicated by the presence of a char layer. The rate constant in both instances, k_t, is related only to the thermodynamic properties of the devolatilizing medium. Once the input flux level, I, is sufficiently high to exceed some minimum threshold level, which is the level required to maintain the surface or reacting regions of the sample at some decomposition threshold temperature, T_s, in the presence of finite loss fluxes to the surroundings, *the process proceeds at a rate determined entirely by the first law of thermodynamics, and no further assumption regarding reaction kinetics is necessary.*

The general viewpoint of a flux-driven pyrolysis and devolatilization wave whose rate of propagation is controlled by the thermal inertia of the reacting system, is also strongly supported by the X-ray density profiles reported by Lee, Singer, and Chaiken (*1*), shown in figure 5, and by their temperature profiles reproduced in figure 4. The X-ray density profiles show that the pyrolysis wave is bounded on the cold side by unreacted coal ($\rho = 1.33$ g/cm^3), and on the hot side by a consolidated char residue ($\rho = 0.85$ g/cm^3). The reaction zone of active pyrolysis and devolatilization is located just above the coal surface and it is characterized by a minimum density of about 0.2 g/cm^3. Recent morphological data obtained with a scanning electron microscope (SEM) at higher laser fluxes, which will be presented in the "Structure Data" section, show clearly that there is a very sharp, discrete transition between the unreacted coal and the char residues from the reaction zone. The transition region shown in figure 5 appears much broader because the heating flux is relatively low and the X-ray densitometer measurements are macroscopic averages over the entire width of the samples, obtained with an instrument with considerably less spatial resolution than is available with the SEM.

In any case, the minimum density zone seen in figure 5 may be viewed as a "fizz zone" of active devolatilization consisting of "frothing" liquid bitumen. The liquid bitumen consists of higher molecular weight pyrolysis products. It is frothing because lower molecular weight gases and tar vapors are bubbling through the liquid. The frothing or bubbling in the fizz zone is physically transporting the frothing mass of charifying liquid bitumen into the mass of previously formed char above it, leaving a low-density region in its wake. The consolidated char is thus a compacted residue of the frothing mass of charifying liquid. As the tar vapors diffuse through that cap of higher temperature char, there are probably also some secondary char-forming reactions occurring in the char layer above the fizz zone. The densitometer traces in figure 5 show clearly that the rate of regression of the pyrolysis wave into sample, $\dot{x}_o$, is decelerating in time as the char layer increases in thickness and temperature, and the net loss flux $I_\ell'(t)$ increases in magnitude. As a result, a smaller fraction of the incident flux is available to drive the pyrolysis wave. That reduction in $\dot{x}_o$ with time is directly reflected in reduction in the $\dot{m}$ values seen in the uppermost curve of figure 2.

Additional evidence for the new mechanism comes from the temperature profiles reproduced in figure 4. The locations of the measured minimum density points are plotted on those profiles and the data show that the minimum density occurs at a fairly constant reaction temperature. Thus, although the instantaneous mass loss rates corresponding to those various profiles vary from as low as 0.08 mg/(cm^2·s) to as high as 0.42 mg/(cm^2·s) the temperature of the reaction zone in which the pyrolysis

and devolatilization process is occurring remains essentially constant at 440° to 475° C. That range of temperatures appears to mainly reflect the uncertainty with which the temperature can be measured and the reaction zone located. There is still too much uncertainty in those measurements to reliably infer that the higher temperature values in that range are associated with the higher rates.

It should be noted from the temperature profile curves shown in figure 4 for the laser flux of 2 cal/(cm^2·s), that the maximum temperature of the char layer at the surface is 760° to 800° C. That surface temperature may be considered to be the source temperature in those experiments since it is the char layer at the surface that directly absorbs the laser flux. Heat is then conducted through that char layer to the reaction zone below. Thus, although the source temperature is 760° to 800° C, the real temperature of the coal surface that is pyrolyzing and devolatilizing is only 440° to 475° C, and it would be incorrect to assign that char layer temperature to the reacting coal. It should also be noted that if the temperature of the solid coal or particle were measured optically from the spectral radiance of the char layer, it would, of course, give only the surface temperature of the char residue and not the temperature of the reacting coal.

SMALL COAL PARTICLE DEVOLATILIZATION RATES AT HIGHER FLUXES

Kinetic data for the devolatilization rates of microscopic Pittsburgh seam bituminous coal particles of varying diameter were obtained by Hertzberg and Ng (*12*). Their data at a constant input laser flux of 300 W/cm^2 for particles of 51-, 105-, and 310-μm diameter are shown in figure 6. The data show clearly that the time required for complete devolatilization increases monotonically with increasing particle diameter, as predicted by equation 8. Hertzberg and Ng also studied the effect of varying the incident laser flux for a given particle size and those data are shown in figure 7. For a given particle size, the time required for complete devolatilization decreases monotonically with increasing laser flux, which is also predicted by equation 8. Equation 8 was derived from equation 7, which is the steady-state expression of the first law of thermodynamics. Thus the particle pyrolysis data of Hertzberg and Ng also support the new mechanism.

For a more careful analyses of their data, it should be noted that their percentage mass loss versus time curves in figures 6 and 7 have characteristic S shapes. The final volatility yields, V(∞), are approached only asymptotically as $t \rightarrow \infty$. Accordingly, it is more accurate to express the rate of the devolatilization reaction in terms of the half-life for devolatilization rather than the time for complete devolatilization. That half-life, $t_{1/2}$, is the time required for the particle to devolatilize to half its maximum value. That $t_{1/2}$ value corresponds to the inflection point of the S-shaped curve, and it is a more representative measure of the rate. All the data of Hertzberg and Ng are summarized in figure 8, where the measured $t_{1/2}$ data points are plotted as a function of the incident laser flux for the three particle sizes studied. For a cubic particle

$$t_{1/2} = \frac{a_o}{2\dot{x}_o} = \frac{a_o \rho \int_{T_o}^{T_s} C(T)dT + \Delta H_v}{2[I(1-r) - I_\ell]} = \frac{a_o \rho}{2k_t [I - I_\ell']} \cdot \quad (14)$$

The cubic particle with edge lengths, a_o, is assumed in equation 14 to be oriented so that one of its faces is perpendicular to the laser beam. If the particle is spherical, or if the orientation with respect to the beam is random, then a geometric correction factor may be required in order to relate a_o to the average particle diameter, D_p. The exact value of the correction factor is related to the shape of the particle, its orientation, its angular reflectance properties, or even its diffraction properties in the limit of very small sizes. In view of those uncertainties, the above assumption with respect to particle shape and orientation is probably as realistic as any, and accordingly one sets $a_o = D_p$ to give

$$t_{1/2} = \frac{0.50\,\rho}{k_t} \frac{D_p}{(I - I_\ell')} = \frac{k'\,D_p}{(I - I_\ell')}. \quad (15)$$

The predictions of equation 15 are shown in figure 8 as the dashed lines labeled theory. The loss flux, I_ℓ', is probably time-dependent even for these small particles; however to a first approximation an average value is taken to characterize the quasi-steady-state loss flux during the devolatilization time. The detailed choices for I_ℓ' are

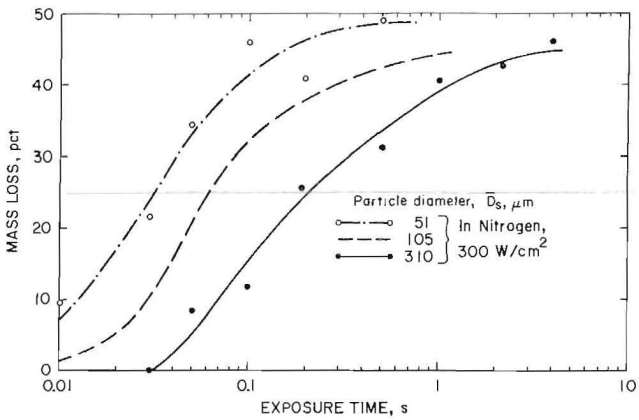

Figure 6.—Devolatilization weight loss for coal particles of 51-, 105-, and 310-μm diameter as a function of exposure time at a constant laser source intensity of 300 W/cm^2, as reported by Hertzberg and Ng (*12*).

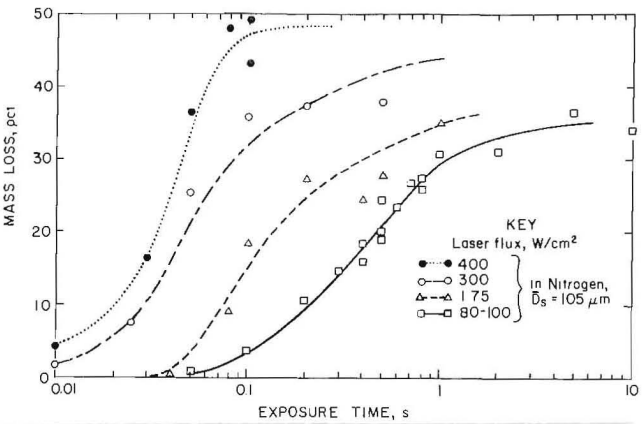

Figure 7.—Devolatilization weight loss for 105-μm-diameter coal particles as a function of exposure time for various laser source intensities, as measured by Hertzberg and Ng (*12*).

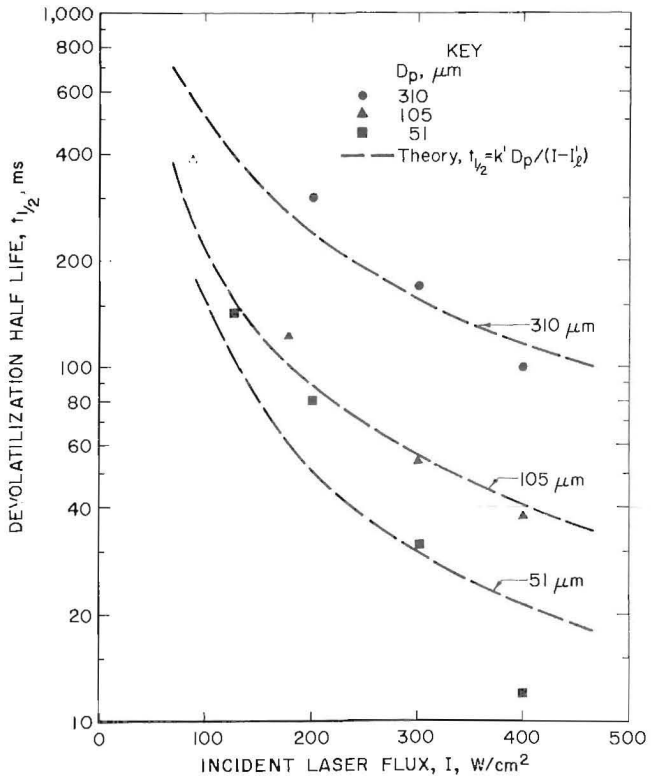

Figure 8.—Summary of measured half lives for coal particles as a function of laser source intensity for three coal particle sizes studied by Hertzberg and Ng (12). Data points are compared with theory based on heat transport limitations according to the first law of thermodynamics.

discussed elsewhere (*12*). For the theory curves shown in figure 8 they were taken as 50 W/cm^2 for the 51-μm-diameter particles, 25 W/cm^2 for the 105-μm particles, and 10 W/cm^2 for the 310-μm particles. They vary inversely with particle diameter because the major loss flux is caused by conductive-convective losses to the ambient cold gas, and that loss flux varies inversely with D_p. A constant k′ value of 1.46 kJ/cm^3 for all three particle sizes gives the best fit to the data points.

The reasonable agreement between the data points and the theory curves predicted by equation 15 tends to confirm the reasonableness of its simple derivation from the first law of thermodynamics. The agreement suggests that even on the microscopic level of particles as small as 50 μm, the devolatilization process proceeds at a rate determined by the speed with which the devolatilization wave is driven through the particle by heat source flux in the presence of heat transport constraints. As with the data previously obtained by Lee, Singer, and Chaiken, the pyrolysis rate constant is related to the thermodynamic properties of the medium and no further assumption regarding a reaction kinetic mechanism is necessary.

Thus the same model of a pyrolysis wave regressing at a rate driven by the absorbing heat flux appears to be as reasonable a description of the small particle devolatilization process as it was of the macroscopic process. For the macroscopic coal samples, the data were obtained at low fluxes of less than 10 W/cm^2 and the time scale for the devolatilization of centimeter-diameter samples was in the range of tens of minutes. At 8 W/cm^2, the maximum mass rate flux of 0.67 mg/(cm^2·s) corresponds to a linear regression rate of $\dot{x}_o$ = 5 μm/s, and the wave takes 2,000 s, or 33 min, to traverse a 1-cm length.

At the much higher fluxes of 100 to 400 W/cm^2, all that appears to be different is that the pyrolysis wave progresses more rapidly into the sample. The temperature profiles steepen and the zone of active pyrolysis and devolatilization becomes much thinner. At 200 W/cm^2, the linear regression rate, $\dot{x}_o$, increases markedly in proportion to the much higher flux: it is 125 μm/s. A factor of 20 increase in incident flux has resulted in a factor of 25 increase in the linear regression rate. At a rate of 125 μm/s, the pyrolysis wave takes only a fraction of a second to travel through a 50-μm-diameter particle.

It is also instructive to compare the thermal loss fluxes, I_ℓ', for small particles inferred from the data of Hertzberg and Ng (*12*) with those previously inferred from the data of Lee, Singer, and Chaiken for large samples. The absolute loss fluxes of 50, 25, and 10 W/cm^2 for the 51-, 105- and 310-μm particles, respectively, are much higher than the loss flux of 4.8 W/cm^2 [1.15 cal/(cm^2·s)] inferred from figure 3 for the large coal sample studies. The loss flux value for the largest of the small particles, 310 μm, is, however, only a factor of 2 larger than for the large-scale coal samples. The comparability in that case is not unreasonable since a 0.31-mm-diameter particle is approaching the size where its boundary layer thickness for heat conduction and convection to the surroundings will tend to become less sensitive to the size of the sample. Although the absolute loss fluxes for the small particle experiments are larger; on a percentage basis, the losses from the small particles are a smaller fraction of the incident flux. The complications associated with the char-layer buildup are relatively less significant for the fine particles than for the larger macroscopic samples.

And finally, one should compare the k_t values obtained from the small particle pyrolysis rates of Hertzberg and Ng with those obtained earlier from the macroscopic pyrolysis studies of Lee, Singer, and Chaiken. A k′ value of 1.46 kJ/cm^3 was inferred from the data in figure 8. From equation 15, one obtains $k_t = 0.50\ \rho/k'$, which gives k_t = 1.91 mg/cal as the Hertzberg and Ng measured value for the pyrolysis and devolatilization rate constant. That value should be compared with the k_t value of 0.75 mg/cal previously inferred from the data of Lee, Singer, and Chaiken. Considering the two orders of magnitude differences in incident fluxes, the three orders of magnitude differences in sample size, and all the other complications and uncertainties involved in the comparison, a difference of only a factor of 2 or 3 in the rate constants is probably the best one may reasonably expect under the circumstances.

Even that difference can be resolved somewhat by considering the reason for the nonlinearity of the $\dot{m}$(max) vs I curve shown in figure 3. As indicated by the tangent line drawn in figure 3, the inferred loss flux is 1.15 cal/(cm^2·s) (4.8 W/cm^2) at an incident flux of 2.0 cal/(cm^2·s) (8.4 W/cm^2). That loss flux is some 60 pct of the incident flux. For the particle pyrolysis data shown in figure 8, the inferred and calculated loss fluxes were a much smaller fraction of the incident flux: from only a few percent for the 310-μm particles at 400 W/cm^2, to at most, 40 pct for the 51-μm particles at 125 W/cm^2. The higher fractional losses from the large samples at the lower fluxes are associated with their thicker char layers and their longer induction times for the onset of devolatilization.

As indicated earlier, the nonlinearity in the $\dot{m}$(max) vs I curve shown in figure 3 is probably caused by the time-dependent thermal losses and the additional thermal inertia of the char layer that develops even during the induction period, τ. Those losses are more severe relative to the incident flux for the macroscopic samples and are probably still very significant even for the data point at 2 cal/(cm^2·s) through which the tangent line in figure 3 was drawn. At higher fluxes, the nonlinearity in figure 3 should eventually disappear and the macroscopic $\dot{m}$(max) vs I curve should become more linear. If one assumes that such a linearity is eventually attained at a final slope that is about a factor of 2 or 3 larger than the tangent line drawn in figure 3, then there would be excellent agreement between the small-particle data of Hertzberg and Ng, and the large, macroscopic pyrolysis results of Lee, Singer, and Chaiken. A single rate constant of about 1.9 mg/cal can thus plausibly characterize the data over two orders of magnitude in incident flux quite independently of particle size: from particles as small as 51 μm to macroscopic samples as large as several centimeters.

The pyrolysis rate constant of k_t = 1.9 mg/cal corresponds to an effective heat capacity for the pyrolysis wave propagation of $\int_{T_o}^{T_s} C\,(T)\,dT + \Delta H_v = 1/k_t = 526$ cal/g. Since the heat capacity integral from ambient temperature to T_s = 450° to 550° C is about 200 to 225 cal/g, the above analysis gives an endothermic heat of pyrolysis and devolatilization for the coal of about ΔH_v = 300 to 326 cal/g.

MACROSCOPIC PMMA PYROLYSIS AND DEVOLATILIZATION

For a polymer such as polymethylmethacrylate (PMMA), the devolatilization of the solid during thermal pyrolysis goes to completion so that there is no char layer left in the wake of the pyrolysis wave. For coal, the data showed that the char layer built up in time and insulated the pyrolysis wave from the heat flux deposited at the charified surface of the sample. For PMMA there is no char layer and the input radiant flux is absorbed directly within the pyrolysis wave front. Thus the laser pyrolysis data for PMMA provide a cleaner test of the new mechanism. The data for PMMA as reported by Kashiwagi and Ohlemiller (*13*) and by Vovelle, Akrich, and Delfau (*27*) at radiant fluxes of 1.4 to 4.0 W/cm^2, in nitrogen, are reproduced in figure 9.

Their instantaneous $\dot{m}$ values can be seen to increase in time during the early stages of pyrolysis and then to level off eventually to some steady-state value at longer times. There is a decline in the $\dot{m}$ values at still longer times, which corresponds either to the consumption of the samples or to increasing flux losses as the back surface of the sample heats up. In the one case (*13*), the samples were 4 by 4 cm square; in the other case they were 10 by 10 cm square. They were subjected to varying input fluxes from a radiant panel or a high temperature, graphite plate. Those exposed square surfaces were oriented *vertically* and the radiant source flux was perpendicular to those exposed square cross sections.

The data in figure 9 should be contrasted with the coal data in figure 2. The coal data at comparable fluxes show a more rapid leveling off followed by a marked decline for comparable exposure times and fluxes. The marked decline in $\dot{m}$ for the coal samples occurs even though the sample is far from being consumed. That decrease in $\dot{m}$ for coal is caused by the thickening char layer buildup, which insulates the unreacted coal from the radiant flux source. For the 4.0-W/cm^2 data of Kashiwagi and Ohlemiller shown in figure 9, it is quite apparent that the exposure times were not long enough to ensure that a steady-state condition was attained; however, for the data of Vovelle, Akrich, and Delfau, a steady-state condition was attained at their longer exposure times.

As just indicated, their decline in $\dot{m}$ for the higher fluxes at still longer times is probably associated with increasing heat losses or sample consumption. A vertical orientation for the exposed surface generates natural convection currents and a vertical, upward boundary-layer flow along the vertical surface. The asymmetry will influence both the consumption rate and the loss flux as time proceeds. The data in figure 9 will be compared with data to be reported here for laser exposure of thermally thicker samples at higher fluxes. The laser data were obtained for conditions that were demonstrably in steady-state and will be compared with the data in figure 9.

But the observation of Kashwagi and Ohlemiller are especially noteworthy because they also simultaneously monitored the surface temperature of their samples during the course of the pyrolysis process. Their temperature data are shown in figure 10, where the measured mass loss fluxes are correlated with the surface temperatures at which those mass losses were measured. Their $\dot{m}$ vs T_s curves are shown for the two radiant flux levels. As indicated earlier, in the absence of a char layer, the radiant source flux is absorbed within the pyrolysis-devolatilization wave front, and the surface temperature is then the temperature of that reaction wave. Their data show clearly that the mass loss rate is quite low until some threshold temperature is approached, at which point the rate becomes very rapid and the $\dot{m}$ vs T_s curve turns vertically upward. The nearly vertical final slope at high

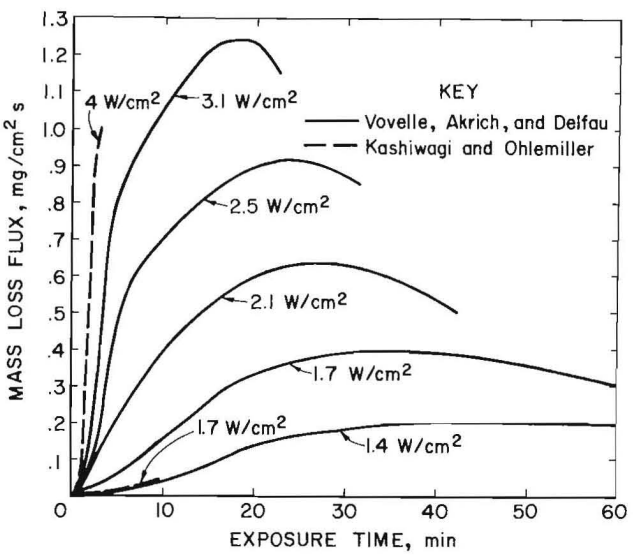

Figure 9.—Pyrolysis and devolatilization mass loss rates of macroscopic samples of PMMA as a function of exposure time as reported by Vovelle, Akrich, and Delfau (*27*) and Kashiwagi and Ohlemiller (*13*).

$\dot{m}$ values means that the rate of pyrolysis and devolatilization has become virtually independent of surface temperature, T_s, once the threshold temperature is reached.

The PMMA surface temperature data in figure 10 are in quite good agreement with the temperature profile data for coal pyrolysis that were shown in figure 4. The coal data showed an essentially constant pyrolysis wave temperature that was quite insensitive to the rate of progression of the pyrolysis wave. For coal, the measured pyrolysis wave temperature was 440° to 475° C. For PMMA, the pyrolysis temperature is also relatively insensitive to the rate, but its value is in the range 350° to 400° C. Both sets of temperature measurements support the general viewpoint that above a critical flux the pyrolysis wave temperature remains relatively low over a wide range of rates, and that its rate of progression into the solid is controlled by the absorbing flux intensity. That critical flux is, in fact, the flux level required for the exposed or reacting surface to reach that reaction temperature in the presence of the loss flux. Although the temperature profile through the pyrolysis zone will steepen at higher fluxes, the temperature within the region of active pyrolysis and devolatilization appears to remain relatively low and insensitive to the rate even as the propagation rate increases markedly.

In order to elaborate further on this interpretation of the data, a theory curve is plotted in figure 10. That theory curve is a simple step function at the reaction temperature, T_s. According to that most simple model, there is no devolatilization in the horizontal portion of the curve ($\dot{m}$ = 0) until the surface temperature of the sample reaches the decomposition temperature, T_s. In order for the exposed surface to reach T_s, a minimum threshold input heating flux is required in order to overcome the loss flux, I_ℓ'. Once the surface reaches the decomposition temperature, T_s, the rate becomes finite and one is in the vertical portion of the step function. The rate is then controlled entirely by the source flux intensity and the temperature of the reacting surface then becomes both invariant and virtually irrelevant. In the vertical portion of the step, the rate

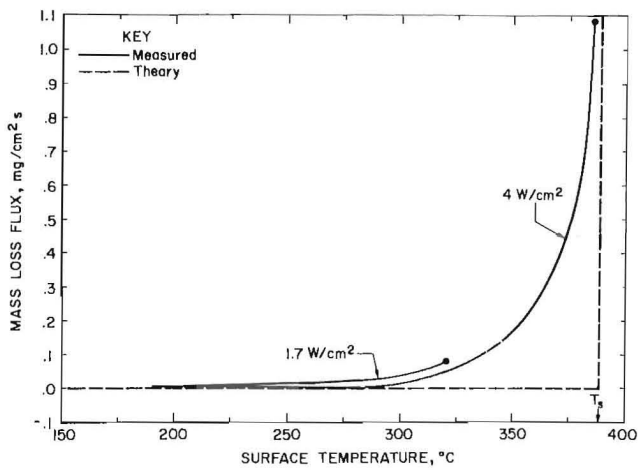

Figure 10.—Measured surface temperatures at various mass loss rates during the pyrolysis and devolatilization of PMMA at two radiant fluxes as reported by Kashiwagi and Ohlemiller (*13*). Measured values compared with simplified, step-function theory using a discrete, decomposition temperature, T_s.

becomes finite, $\dot{m} > 0$; however, its magnitude is controlled by the external flux supply level and thermal transport constraints.

The simplest model thus uses a step function to approximate the finite curvature of the transition depicted in figure 10. Clearly, the system is, in fact, under kinetic rate control in the horizontal portion of the step but only while nothing is happening and $\dot{m} = 0$. More precisely, something is actually happening in the horizontal portion of the step, namely the surface is heating up in the input flux, but there is no devolatilization occurring because the temperature is too low. The system is clearly under kinetic control in that horizontal portion of the step; however, as soon as something happens and significant pyrolysis and devolatilization begins, one transits into the vertical portion of the step where the system is under heat transport control.

Clearly, one must condede that the data curves in figure 10 do, however, show finite curvature rather than the discontinuous step function. Accordingly, one might be tempted to argue that there is a region of temperatures below T_s where the system could be under kinetic rate control at low but finite reaction rates. There are, however, many other possible reasons for the finite curvature.

The normal mass density discontinuity at the phase boundary between a solid and a gas is truly discontinuous on dimensional scales larger than atomic dimensions; yet, if one attempts to measure that spatial step function in mass density with an instrument whose spatial resolution is not adequate to reveal that sharp discontinuity, the result will be a blurring of the interface and the step function density discontinuity will appear to have a finite curvature. Thus, the measured curvature in the temperature profiles in figure 10 may simply reflect the finite thickness of the thermocouple used to make the temperature measurement and/or the uncertainty in defining or locating the true surface of the phase discontinuity between the condensed phase reactants and their gaseous products.

The studies of Kashwagi and Ohlemiller show that the devolatilizing surface of PMMA is not actually a phase discontinuity of infinitesimal thickness. The reaction zone exists in the form of a bubbling zone of finite thickness, and their measuring thermocouple was probably located at the outermost surface of the bubbling zone. A thermocouple of finite thickness in a bubbling zone of finite thickness through which there is a finite temperature gradient will register some average temperature that will inevitably smooth out any of the discontinuities that may exist across the walls of the individual bubbles.

The finite thickness of the bubbling zone is a reflection of mass transport limitations as well as heat transport limitations. Subsurface bubbles within which devolatilization may have already occurred must first overcome the viscous resistance of the melt and its surface tension forces in order to reach the macroscopic surface and release their vapor contents. It is not until these bubbles reach the macroscopic surface that the devolatilization process, which may have already occurred across the bubble wall, can be registered as a finite increment in Δm. The finite curvature in $\dot{m}$ vs T_s could thus be a reflection of that finite bubbling zone thickness whose presence is caused by a mass transport limitation rather than a kinetic rate limitation. The true $\dot{m}$ vs T discontinuity across the bubble wall dimensions, and on the microscopic $\dot{m}$ scale of each bubble, could actually reveal a more discontinuous

transition than the macroscopic average measured in figure 10.

In any case, for whatever reason the finite curvature exists in figure 10, the curves shown there are for low incident fluxes of 1.7 and 4.0 W/cm^2. The maximum $\dot{m}$ value at the highest flux was only about 1 mg/(cm^2·s). Those fluxes barely exceed the threshold value required to overcome the loss flux. For incident fluxes of 100 to 400 W/cm^2, the corresponding $\dot{m}$ values are in the range of 25 to 100 mg/(cm^2·s). If the curves in figure 10 were plotted on that larger $\dot{m}$ scale, the finite curvature would be barely visible, and the step function would be an accurate representation of the curves.

It should be conceded that if the surface temperature were precisely known, the $\dot{m}$ versus T curve would most likely not have an infinite slope at a finite T_s value. Thus T_s probably increases somewhat as the driving flux and $\dot{m}$ increase. There is a hint of such behavior in the PMMA data, and also in the temperature profiles of Lee, Singer, and Chaiken. But, the important point to realize is that in this flux-driven, heat-transport-limited model, once the flux level exceeds the critical value for the onset of significant reaction, the predicted rate is not particularly sensitive to the choice of the surface or reaction temperature, T_s. That temperature is only the upper bound of the heat capacity integral. For PMMA, for example, an increase in T_s from 350° C to 550° C would, according to equation 7 or 13, decrease the rate constant, k_t, by only about 30 pct.

By contrast, in the traditional viewpoint of kinetic rate control, as expressed by equations 2, 3, and 4, the reaction temperature, T_s, is the *only* variable that determines the rate of pyrolysis and devolatilization.

In the flux-driven, heat-transport-limited model being presented here, the system is highly nonisothermal and is driven by thermodynamic constraints. In such a nonisothermal system of coupled heat and mass transport, the exact temperature of the surface or the phase discontinuity becomes virtually irrelevant. The driving force for the reaction is not the temperature of the pyrolysis zone. The driving force cannot be the value of an *intensive* variable in one particular region of the system, especially when there are large gradients in that intensive variable. The driving force is an *extensive* variable, the net energy power density ($I - I_\ell'$) passing into and through the surface and being absorbed by the reactant. It is that extensive variable that is the driving force controlling the reaction rate. The barrier to the reaction is not some activation energy, E_a, which must be overcome by raising the temperature of one particular region of the system to a high enough level; rather, it is the resistance or thermal inertia of the entire system that must be overcome, and that thermal inertia is $\int_{T_o}^{T_s} C_p(T)\,dT + \Delta H_v$. In this model of thermodynamic control, the reciprocal of that resistance is the conductivity of the medium to the reaction wave, which is its rate constant, k_t.

The PMMA devolatilization rate data presented in figure 9 are further analyzed in figure 11. The measured maximum mass loss fluxes or devolatilization rates per unit area are plotted as a function of the input heat fluxes. Separate straight lines are drawn through the data points of Vovelle, Akrich, and Delfau and those of Kashiwagi and Ohlemiller. The analyses, for the moment, will ignore the reflectance loss flux, rI, by assuming that it is negligible in comparison to I_ℓ'. The equation representing the straight line obtained from the data of Vovelle, Akrich and Delfau is $\dot{m}$ [mg/(cm^2·s)] = k_t ($I - I_\ell'$) = 0.631 (mg/J) [I − 1.07] (W/cm^2). Such a straight line can fit directly to equation 12 and the inferred loss flux for the PMMA pyrolysis experiment is therefore I_ℓ' = 1.07 W/cm^2. The measured rate constant for the pyrolysis and devolatilization process is therefore k_t = 0.631 mg/J, which is equal to 2.640 g/kcal. Its reciprocal, $1/k_t$ = 379 cal/g, is, according to equation 13, the thermal inertia of the pyrolysis and devolatilization wave, $\int_{T_o}^{T_s} C(T)\,dT + \Delta H_v$.

Data for the heat capacity of PMMA at room temperature and elevated temperatures have been reported by Bares and Wunderlich (*28*). The room temperature heat capacity is 0.33 cal/(g·K), and it increases almost linearly to a value of 0.62 cal/(g·K) at 350° C. From the surface temperature measurements shown in figure 10, one can infer an average pyrolysis wave temperature of T_s = 350° C. Evaluating the heat capacity integral for PMMA from ambient temperature to that value of T_s, gives $\int_{25^\circ C}^{350^\circ C} C(T)\,dT$ = 164 cal/g. Subtracting that 164 cal/g from the measured total thermal inertia of 379 cal/g gives ΔH_v(PMMA) = 215 cal/g. That value compares very favorably to the sum of the heat of depolymerization of PMMA into its monomer, which is reported (*29*) to be 137 cal/g,

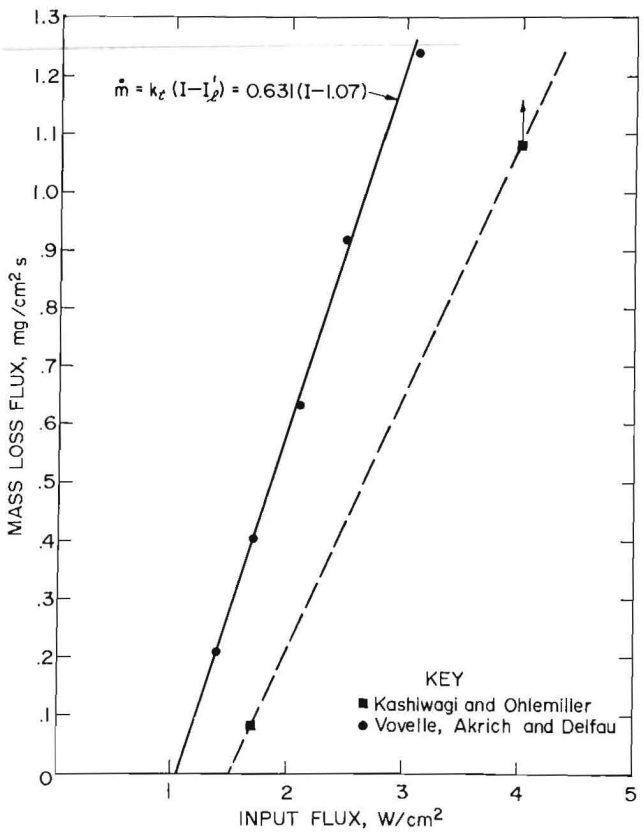

Figure 11.—Measured maximum devolatilization rates for PMMA as a function of incident source flux intensity from data reported in references 13 and 27.

and the heat of vaporization of the monomer, which is calculated to be about 80 cal/g according to Trouton's rule.

Although the maximum $\dot{m}$ values of Kashiwagi and Ohlemiller are also shown in figure 11, it is clear from figure 9 that their devolatilization rate at 4.0 W/cm^2 does not yet represent a steady-state value for $\dot{m}$. Comparison of their data with those of Vovelle, Akrich, and Delfau show that their steady-state $\dot{m}$ value would most probably be considerably higher than the plotted value of 1.08 mg/(cm^2·s) if they had attained a steady-state condition. Accordingly, that point is plotted with an upward arrow suggesting that its true value is higher. That higher value suggests that the slope inferred from the corrected data of Kashiwagi and Ohlemiller would probably be in better agreement with that obtained from the data of Vovelle, Akrich, and Delfau. Comparison of the two lines, however, shows clearly that the loss flux for Kashiwagi and Ohlemiller data is considerably higher at about 1.50 W/cm^2 compared with 1.07 W/cm^2 for Vovelle, Akrich, and Delfau. That is not surprising since the Kashiwagi and Ohlemiller samples were smaller, 4 by 4 cm, as opposed to the 10- by 10-cm samples of Vovelle, Akrich, and Delfau. Smaller samples would be expected to have a higher convective loss flux component.

The data shown in figure 11 were all obtained at relatively low fluxes, and the loss flux levels of 1.07 and 1.50 W/cm^2 respectively, were a large fraction of the incident fluxes of 1.4 to 4.0 W/cm^2. As a result, the times required to achieve a condition of steady-state devolatilization were quite long. In addition, the samples were relatively thin (1.5 cm thick) in comparison to the pyrolyzing areas of 4 by 4 cm and 10 by 10 cm. At such low fluxes and long exposure times, such geometrically thin samples can also become thermally "thin" in the sense that there is considerable opportunity for heat to accumulate on the back surface of the sample. As the exposure time increases in such a sample and it becomes thermally thin, the initial temperature of the reactant mass will increase to above the ambient temperature, T_o, and because of that continuous heat accumulation, a true steady-state condition becomes more difficult to achieve.

In addition, the vertical orientation of the samples induces a vertical asymmetry as a result of natural convection. Hot pyrolysis gases rise upward by buoyancy and induce an upward flow of entrained cold air parallel to the exposed surface. That induced cold-air flow stream can approach quite close to the pyrolyzing surface near the bottom edge of the sample and cool it readily. As one moves upward toward the top edge of the sample, there is an accumulating flow of pyrolysis gases that generates a thickening boundary layer, which effectively shields the upper regions from the entrained flow of cooling air; and this diminishes the convective heat flux loss near the top of the sample. Clearly, in such a vertical orientation there is a vertical temperature asymmetry which induces a vertical gradient in the loss flux. There is little doubt that the induction time required for the surface to reach the pyrolysis temperature will be longer near the bottom of the sample than near its top and that the upper regions will pyrolyze at a higher rate.

In view of those uncertainties, it was decided that independent experiments should be performed with PMMA at much higher flux levels. The laser pyrolysis apparatus previously used by Hertzberg and Ng (*12*) for coal particle pyrolysis was modified to obtain a more uniform spatial distribution of the output flux. Cylinders of PMMA with a diameter of 0.45 cm were subjected to a laser flux that was incident on the flat, top surface of the cylinder. Long cylinders were used whose lengths were substantially larger than the diameter. The samples were oriented such that the pyrolyzing surface was horizontal and the laser beam was incident vertically from above. The pyrolysis wave front then propagated downward along the axis of the cylinder. The weight loss per unit area, Δm, was measured as a function of exposure time in a given laser flux. The data are summarized in figure 12. The good linearity of the Δm vs t curves clearly indicate that steady-state conditions were obtained for these thermally thick samples at the higher laser fluxes.

The least squares linear fits to the data points are very well represented by the equation

$$\Delta m = \alpha (t - t_o) \simeq \dot{m} (t - \tau), \qquad (16)$$

where the slope of each line, $\alpha = \dot{m}$, is the steady-state devolatilization rate at each flux. The horizontal intercept, $t_o = \tau$, is simply the induction time at that flux. The induction time, as indicated earlier, is the time required for the surface to be heated to the devolatilization temperature. The slopes and intercepts obtained from the least squares fits to the data points at each flux level are summarized in table 1. Those measured, steady-state

Table 1.—Least squares fit to data for pyrolysis and devolatilization weight loss of PMMA at various laser flux levels

Δm (mg/cm^2) = $\dot{m}$ [mg/(cm^2·s)] [t − τ] (s)

Input laser flux, W/cm^2		Mass loss flux	Induction time,
Incident (I)	Net, I(1 − r)	($\dot{m}$), mg/(cm^2·s)	(τ), s
115	107	70.0	0.101
70.7	65.8	40.1	.160
42.5	39.5	21.8	.499
23.2	21.53	9.92	1.83
12.4	11.53	1.54	6.66

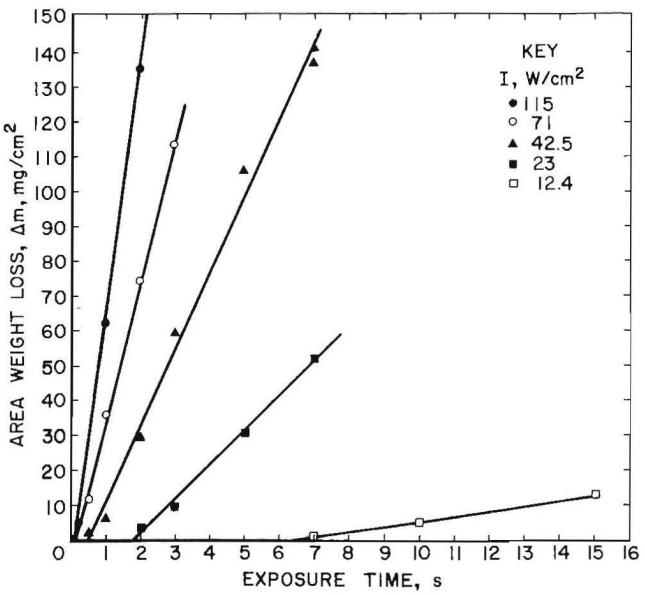

Figure 12.—Measured pyrolysis and devolatilization weight losses for 0.45-cm-diameter PMMA cylinders as a function of exposure time for different input laser flux intensities in the range 12 to 115 W/cm^2.

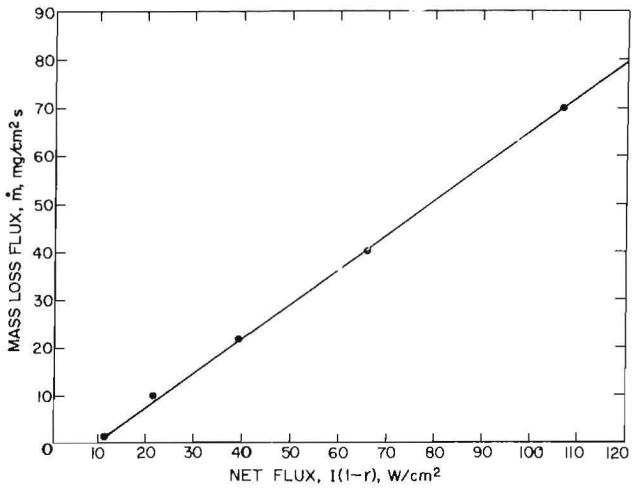

Figure 13.—Measured steady-state rates of pyrolysis and devolatilization for 0.45-cm-diameter PMMA cylinders, as a function of input laser flux corrected for surface reflectance, r.

devolatilization rates are plotted in figure 13 as a function of the net incident flux I(1 – r).

The data are now considered to be sufficiently accurate so that an explicit correction for the reflectance loss should be made. In the previous analysis, the range of flux measurements and the accuracy of the ṁ values were not sufficient to justify that explicit correction for reflectance losses, and its value was simply included in I_ℓ'. The data in figure 12 are now sufficiently accurate and the order of magnitude range of the flux measurements is such that an explicit reflectance correction is justified. The magnitude of the reflectance loss, rI, increases with increasing flux, and hence it cannot be accurately included in a constant I_ℓ', especially when it varies by such a large extent. The reflectance loss for PMMA is taken as 7 pct, which gives r = 0.07 and (1 – r) = 0.93. A least squares fit to the data points in figure 13 is represented by the equation

$$\dot{m}\ [\mathrm{mg/(cm^2 \cdot s)}] = 0.72\ (\mathrm{mg/J})\ [0.93\ I - 9.8](\mathrm{W/cm^2}). \quad (17)$$

The inferred, steady-state loss flux for these samples is therefore $I_\ell' = 9.8\ \mathrm{W/cm^2}$. These smaller samples of 0.45-cm diameter thus display a loss flux of about 10 W/cm² compared with the loss flux of 1.5 W/cm² inferred from the data for the 4- by 4-cm samples. A black body at the PMMA surface temperatures would reradiate 1.2 W/cm². If the emissivity of PMMA is taken to be at about 0.8 in the far infrared, the reradiative loss flux is only about 1.0 W/cm². That reradiative loss accounts for most of the loss flux for the 4- by 4-cm-square samples used by Kashiwagi and Ohlemiller.

By contrast, for the much smaller 0.45-cm-diameter rods used here, reradiation accounts for only about 10 pct of the loss flux. Clearly the major loss flux from the smaller samples is by conduction and convection to the cold surrounding. These smaller samples have a much larger surface area per unit volume of the devolatilization zone, and hence they are expected to have a larger loss flux by conduction and convection to the cold surroundings.

The magnitude of the purely convective loss flux can, in fact, be estimated rather simply. One can simply estimate the vertical, buoyant velocity induced by the heated surface using the classical Froude number derivation. One considers the gravitational potential energy, $\Delta\rho\ g\ d$, of a gas volume with characteristic dimensions, d, having a density difference, $\Delta\rho$, between it and its surroundings. That density difference induces a convective flow whose kinetic energy is $1/2\ \rho\ v_b^2$. Equating that gravitational potential energy with buoyancy induced kinetic energy and solving for the corresponding buoyant convective velocity gives $v_b = [2\ g\ d\ \Delta\rho/\rho]^{1/2}$.

For the samples used, d = 0.45 cm. Setting $\Delta\rho/\rho = (T_s - T_o)/T_s = 0.56$, and substituting into the above solution gives $v_b = 22$ cm/s. That buoyancy-induced flow velocity above the sample convects heat upward from the sample to the surroundings. That heat flux loss to the surroundings is simply given by I_ℓ' (convection) = C(air)ρ v_b ($T_s - T_o$). For heated air at the surface temperature of 400° C (673 K), C(air) = 1.09 J/(g·°C) [= 0.26 cal/(g·°C)], $\rho = 0.52 \times 10^{-3}$ g/cm³, and one obtains I_ℓ' (convection), = 5 W/cm². If one adds a reradiative loss of 1 W/cm² to that value, one is left to infer a purely conductive loss flux of 3.7 W/cm² to add up to the measured value of 9.7 W/cm². This comparison of calculated to measured loss flux appears to be reasonable.

Although the absolute magnitude of the loss flux is larger for these smaller diameter samples, those losses represent a much smaller fraction of the incident flux, especially for the high flux data points shown in figure 13. Thus at an incident flux of 115 W/cm², the losses rI + I_ℓ' = 17.9 W/cm², represent only 16 pct of the incident flux.

Even for the data point in table 1 for I = 12.4 W/cm², where the net loss flux, rI + I_ℓ' = 10.67, represents some 85 pct of the incident flux, the linearity of its Δm vs t curve (fig. 12) shows clearly that a steady-state condition was nevertheless attained for times longer than its induction time of $\tau = 6.66$ s.

Such steady-state conditions were obtained for all the Δm vs t curves shown in figure 12. The measured rate constant of 0.72 mg/J does, in fact, compare favorably with the slope obtained from the data of Vovelle, Akrich, and Delfau plotted in figure 11. If their value is corrected for the same reflectance loss, their slope at low fluxes corresponds to a rate constant of 0.67 mg/J. The value obtained from figure 13 of $k_t = 0.72$ mg/J corresponds to 3.01 g/kcal. Its reciprocal, $1/k_t = 332$ cal/g, is, according to equation 13, the thermal inertia of the pyrolysis and devolatilization wave $\int_{T_o}^{T_s} C(T)\,dT + \Delta H_v$. The data reported in figure 13 thus correspond to a somewhat higher value for the rate constant than that reported by the data of Vovelle, Akrich, and Delfau shown in figure 11.

In addition to the surface temperatures shown in figure 10, Kashiwagi (*30*) had earlier reported a fairly constant PMMA temperature of 375° to 410° C for a wide range of laser fluxes between 8 and 20 W/cm². Using his average value, but weighted toward the higher temperatures in that range because of the higher fluxes used in these experiments, one takes T_s = 400° C. Use of the same heat capacity data of Bares and Wunderlich (*28*) for PMMA gives $\int_{25°\ C.}^{400°\ C} C(T)\,dT = 196$ cal/g. Subtracting that value from the total thermal inertia of 332 cal/g gives ΔH_v (400° C) = 136 cal/g.

That value for the heat of devolatilization of PMMA inferred from the rate data in figures 12 and 13 is now

significantly lower than that calculated thermodynamically from the sum of the measured heat of depolymerization (*29*) and the estimated heat of vaporization of the monomer. The entire thermodynamic cycle involved in going from the solid polymer at 25° C to the monomer vapor at 400° C, follows.

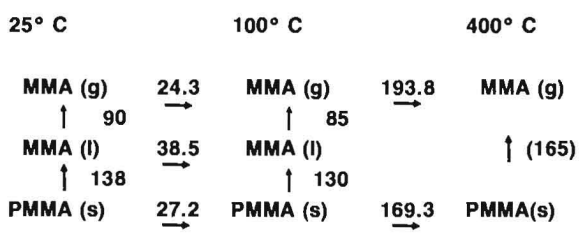

The numbers written along the arrows are the enthalpy changes, in calories per gram, for each transition, and they are estimated from a variety of sources (*28–29, 31*). A variety of paths can be taken in going from the solid polymethylmethacrylate polymer, PMMA (s) at 25° C, to the methylmethacrylate gaseous monomer, MMA (g) at 400° C. The several paths give total enthalpy changes for the transition that are as low as 362 cal/g and as high as 455 cal/g. Clearly there can be only one correct value for the enthalpy change for the transition: PMMA (s), 25° C → MMA (g), 400° C. Based on an evaluation of the available data, it is here estimated that 380 cal/g is the best available thermodynamic estimate of that enthalpy change.

The measured value for that enthalpy change obtained from the pyrolysis rate data in figures 12 and 13 is 332 cal/g. Another measured value can be obtained from the data of Vovelle, Akrich, and Delfau shown in figure 11. If their data are corrected for the reflectance loss, their rate constant becomes 0.67 mg/J, which corresponds to a measured enthalpy change of 360 cal/g. Their data are thus in somewhat better agreement with the thermodynamically calculated value of 380 cal/g. But clearly both measured values give enthalpy changes that are lower than the thermodynamic value by about 13 and 5 pct, respectively. The measured rate constants, which are the reciprocals of that enthalpy change, are thus somewhat higher than the thermodynamic prediction. One possible reason for the higher measured value is the mass loss of fine liquid droplets that may be ejected from the bursting bubbles in the liquid monomer melt. Such a mass transport loss would not require that the heat of vaporization of the monomer be supplied by the external source flux, to that fraction of the mass that is lost as droplets, and that is sufficient to account for the major difference between measured and calculated values. It is also possible that the Vovelle, Akrich, and Delfau data are more accurate than those reported here because they were obtained from instantaneous mass loss rates after steady state had been achieved. Such instantaneous $\dot{m}$ measurements are insensitive to the thermal persistence of the pyrolysis wave. The data reported in figures 12 and 13 are uncorrected for that persistence effect in which the wave will continue to propagate for a small time interval after the laser is turned off. As a result, the measured mass loss will be higher than the true mass loss for that laser exposure time. That effect could account for the small difference between the data of Vovelle, Akrich, and Delfau, and the measurements reported here.

Considering both sets of measurements, there is clearly fair agreement between them and the expectations of thermodynamics. There is thus strong support for the argument that the devolatilization rate process is heat-transport-controlled by a rate constant whose value is given by the reciprocal of the thermal inertia of the system. That thermal inertia is simply the enthalpy change for the overall heating and devolatilization process.

STRUCTURE DATA

The devolatilization rate data just presented for coal particles and for larger macroscopic samples of both coal and PMMA, have supported the viewpoint that the process occurs in the form of a nonisothermal devolatilization wave front whose propagation rate is heat-transport controlled. In this section, independent data will be presented of a structural nature, which clearly reveal the morphology of that wave front for both fine coal particles and for the macroscopic coal samples. The structural data are in the form of scanning electron microscope (SEM) photomicrographs obtained from samples exposed to the laser heating flux.

Since the samples are initially isothermal and at ambient temperature, the first phase of the pyrolysis and devolatilization process is a non-steady-state heating process: a finite induction time is required for the surface to reach the decomposition temperature. During that induction time, a subsurface temperature profile is also developed within the sample since the mass has a finite thermal conductivity. The devolatilization rate is zero during that induction time, τ, and that first phase is clearly seen in the data in figure 12. The second phase is a steady-state process: the pyrolysis and devolatilization proceeds and it does so at a linear rate as the temperature profile, developed during the first phase, propagates into the sample and consumes it at a constant linear velocity, $\dot{x}_o$. That second process is also clearly revealed from the linear slopes of the curves in figure 12, for times longer than τ.

The data in figure 12 were for PMMA, a completely devolatilizing polymer. Although coal is complicated by the presence of a char layer, the macroscopic data for coal shown in figure 4 also support that general viewpoint. They reveal a low-density reaction zone propagating inward at a nearly steady-state rate, impeded somewhat by the presence of an ever-thickening char layer. For fine coal particle devolatilization, the microscopic rates of devolatilization were also consistent with such a linearly propagating pyrolysis wave front. They showed a particle size dependence that was consistent with such a linear velocity

whose magnitude was controlled by the laser source intensity and the thermal heat transport constraints *within* the particle.

But such rate data are only indirect evidence. It is natural to ask whether there is any direct *visual* evidence for the existence of such a devolatilization wave front. If such a wave front exists, what is its thickness? Its existence for macroscopic coal samples is shown from the X-ray radiographic data in figure 4. The wave front thickness there appears to be about 1 to 2 mm. But what if the particle size is much smaller than that dimension? It is argued by advocates of the traditional, kinetic rate control mechanism, that if the particle is small enough (relative to the wave front thickness) then it would be reasonably valid to assume that it reacts isothermally and uniformly throughout its extent.

This section is devoted to a direct exploration of those issues through the presentation of structural evidence obtained from microscopic observations. The data were obtained in the form of SEM photomicrographs. They record the morphological changes in coal structure induced by its heating and devolatilization during laser beam exposure. The details of the SEM used to obtain the data and the experimental methodology were described elsewhere (*12, 32*).

COAL PARTICLE SEM DATA

The SEM photomicrographs shown in figure 14 are for a 310-μm-diameter, Pittsburgh seam bituminous coal particle exposed for 100 ms to a laser flux of about 100 W/cm^2. The same particle is shown at two different magnifications. The measured weight loss was only about a percent or so, and one can thus infer that the exposure time barely exceeded the induction time. There is nevertheless clear evidence that liquid bitumen was formed near the surface of the particle. That bitumen was oozing out from between the bedding planes while the particle was being heated, but after the beam was turned off, the surface cooled and the bitumen resolidified in the form of ridges. Those ridges are clearly seen to be oriented parallel to the bedding planes. A few blowholes are visible in those ridges of resolidified bitumen, but there are many more unbroken bubbles containing volatiles that were probably never emitted from the heated surface. Most of those volatiles have probably recondensed as liquid tars that are still contained within the bubble enclosures. Clearly, although devolatilization may have occurred within those bubbles, the process was not yet registered as a weight loss since the volatiles never broke through the bubble walls.

The SEM photomicrographs in figure 14 suggest that the extent of thermal pyrolysis in a particle may be more extensive than what is revealed from the devolatilization weight loss. In order to be more precise, one should therefore distinguish between those two sequential processes. Pyrolysis or decomposition occurs first and volatile emission occurs afterwards. The SEM photomicrographs in figure 14 clearly illustrate the nature of the mass transport limitation involved in the transition between the generation of volatiles by thermochemical pyrolysis and their subsequent emission by bubble transport and rupture. It is only after the latter process is complete that a finite weight loss is registered.

The SEM photomicrograph shown in figure 15 for a different particle reveals a later stage in the particle devolatilization process. It is also a high volatile, Pittsburgh seam bituminous coal particle, but the morphological changes are more extensive and revealing. It is also a

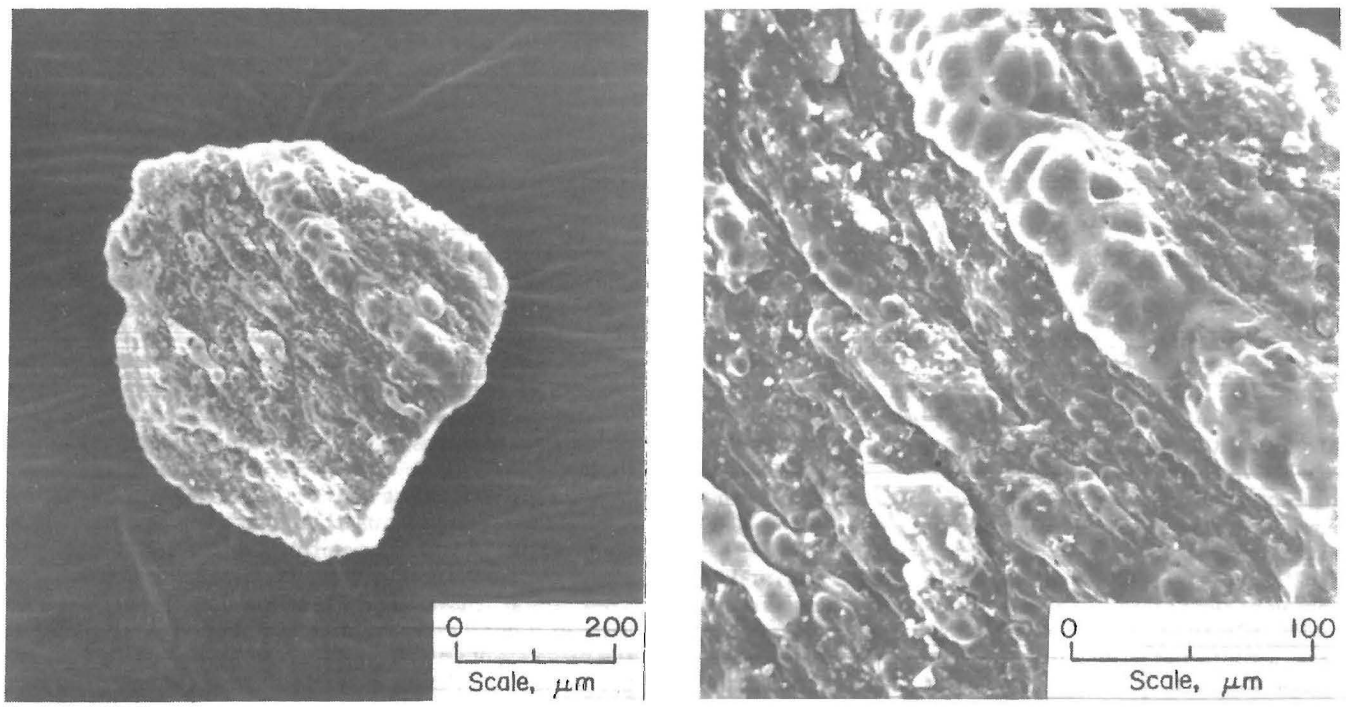

Figure 14.—SEM photomicrographs of exposed surface of 310-μm-diameter coal particle exposed for 100 ms to a laser flux of about 100 W/cm^2, seen at two magnifications.

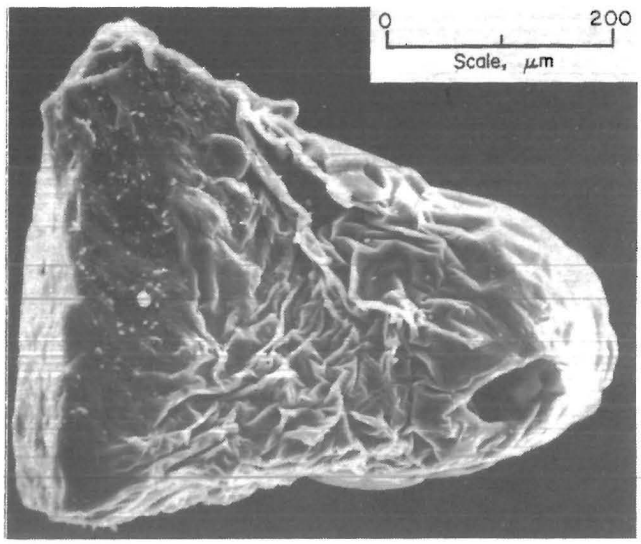

Figure 15.—SEM photomicrographs of a 310-μm-diameter coal particle, which is about two-thirds devolatilized after exposure for 400 ms to a laser flux of about 125 W/cm^2.

310-μm particle, but it was exposed for 400 ms at a laser flux of about 125 W/cm^2. The exposure was in air in this instance, but for these shorter exposure times it is irrelevant whether the exposures is in air or pure N_2 (*12*). The particle was somewhat more than half devolatilized; that is, the measured weight loss was about 23 pct for a particle whose maximum volatile yield was 36 pct at that flux. The particle has clearly not reacted uniformly throughout its extent. Only the upper half of the particle, seen in figure 15 as its right-hand side, has devolatilized. The lower half of the particle (on the left) is essentially unreacted; it is the original coal structure. The laser beam was incident on the upper surface of the particle and only the upper portion was devolatilized during the exposure time. It devolatilized into a dome or bubble, and after the volatiles contained within that dome were vented through blowholes, the whole structure seems to have started to collapse under its own weight. But, as it was collapsing, the higher molecular weight pyrolysis products that compose the dome wall were simultaneously solidifying into a char. When they did solidify, a wrinkled skin residue was left. Those wrinkles reveal the direction of the gravitational force under which the dome collapsed once the pressure force of the lower molecular weight volatiles was relieved by venting.

The devolatilization wave thus appears to have traversed more than half way through the particle when the laser beam was turned off. The particle then cooled and the devolatilization process was quenched with the pyrolysis wave frozen in place. Clearly the thickness of the pyrolysis and devolatilization wave front is substantially smaller than the particle diameter. One can infer a wave front thickness of no more than 50 μm from the SEM photomicrograph in figure 15. Clearly the wave front thickness is a function of the source flux intensity. While the X-ray radiographs in figure 4 give a thickness of about 1,000 μm (1 mm) for a source flux of 8 W/cm^2, the SEM photomicrograph in figure 15 gives a wave front thickness of less than 50 μm for a source flux of 125 W/cm^2. Thus the thickness of the pyrolysis wave front appears to be an inverse function of the source flux intensity that drives the wave, as would be expected.

In interpreting the SEM data shown in figure 15, one must realize that there is, of course, some thermal inertia in the wave front so that its progression does not stop instantaneously after the laser source is turned off. A finite time is required for that temperature profile or preheat stored in the pyrolysis wave to dissipate and decay, especially if it is also being driven by the temperature gradient and thermal inertia in the char layer above it. The wave will thus progress to some extent during that decay time. There has been no attempt to correct for that effect in the rate data presented earlier. The wave front may also thicken to some extent during that quenching time, so that the wave thickness registered by the quenched, dead wave may, in fact, be somewhat broader than for an active, live wave.

Despite that complication associated with the thermal inertia of the system, if the exposure flux for a given particle size is carefully adjusted and timed, the process is readily frozen as the wave propagates through only a portion of the particle's diameter, such as was the case for the particle in figure 15. Similar examples of such partially devolatilized particles are shown in figure 16. Those particles are about 200 μm in diameter and were exposed to a laser flux of about 100 W/cm^2, in nitrogen, for about 1 s. Their average weight loss was about 25 pct, so that they were about two-thirds devolatilized. In all four instances, the particles are viewed from the top; which was the upper surface on which the laser beam was incident. The blowholes and char residues are seen on the top portions of the particles, while the unreacted coal residues with their cleaved edges and ledges are clearly visible at the bottom. Again, the pyrolysis waves are frozen in place after having transversed only a part of the way into the particles.

It should be noted that such partially devolatilized particles with the wavefront frozen in place about half way through the particle, are readily observable in these laser heating experiments because the exposure to the heat flux is *uni*directional. The laser beam is incident from only one direction, and if the particle is approximated as spherical, that laser flux is incident only on its *projected* area, πa_o^2. In a drop furnace, however, or in a flame reactor, the heat flux is *omni*directional. For the drop furnace or flame reactor, the heating flux is incident on the entire surface area, $4\pi a_o^2$, of the particle. For the omnidirectional case, the pyrolysis wave is initiated simultaneously over the entire surface of the spherical particle and the unreacted coal is always hidden from view by the char layer residue that is left in the wake of the wave. For such omnidirectional exposure one would have to slice or section the particle in order to see the unreacted coal core at its center. In addition, the thermal inertia effects discussed above become much more significant for the omnidirectionally heated particle than for the particle that is unidirectionally heated in a laser beam.

A pyrolysis and devolatilization wave once established on the entire external surface area of a spherical particle will progress inward and converge to the center from all directions. Such a self-converging, spherical, pyrolysis wave surrounded by a surface layer of hotter char contains much more thermal inertia per unit mass of unreacted coal than a planar, unidirectional wave. The spherical, inward converging wave will therefore progress much further by its thermal inertia after the source is turned off. In addition, the inward propagating spherical wave front

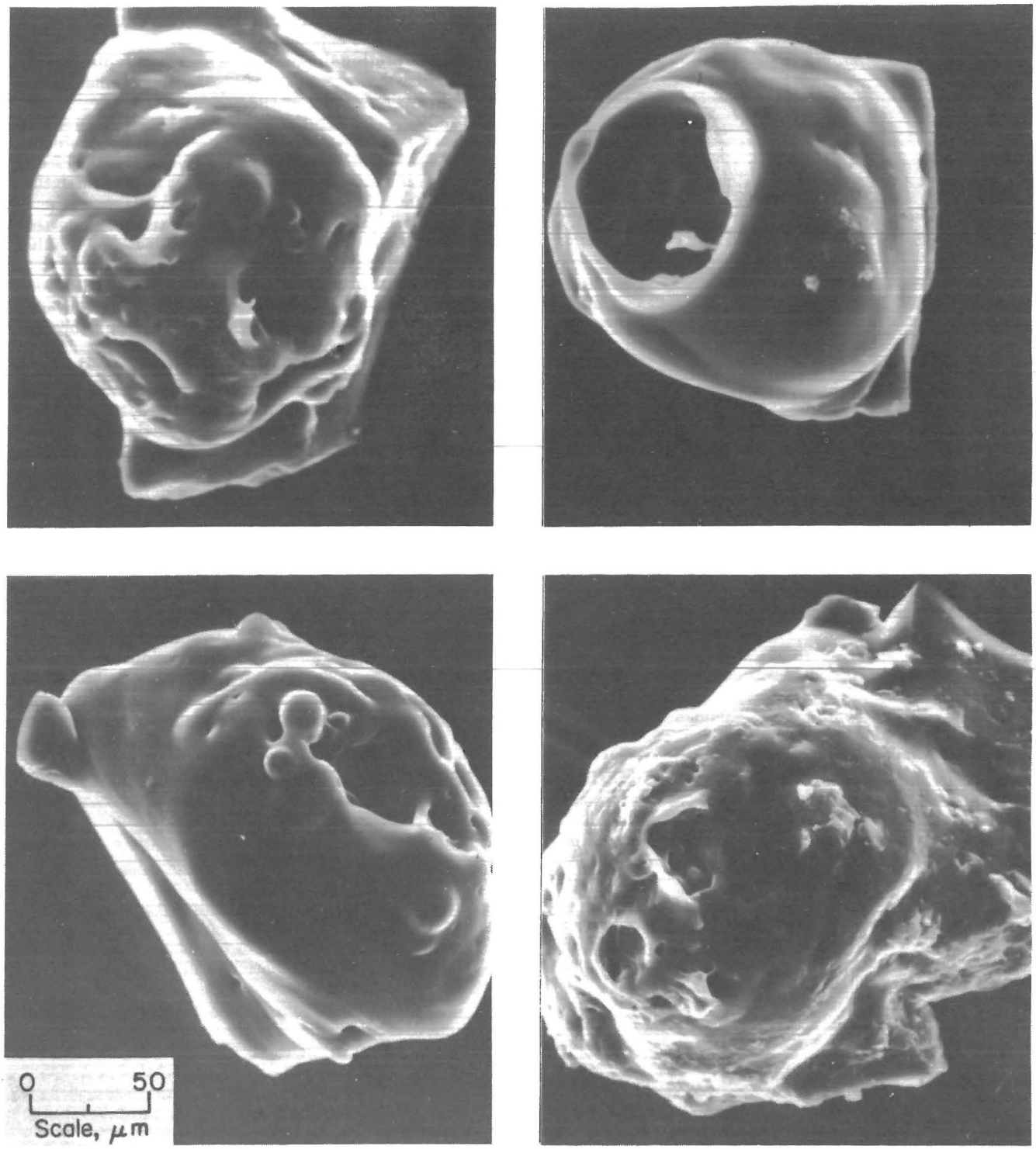

Figure 16.—SEM photomicrographs of four different 200-μm-diameter particles exposed to a laser flux of about 100 W/cm^2 for 1 s. Particles are all about two-thirds devolatilized by laser flux incident, as seen from above.

is more adiabatic. It cannot cool as rapidly because it is completely contiguous and self-contained. It has no edges that are in direct contact with the cold surroundings. The inward propagating, spherical wave can lose heat to the surroundings only from its enveloping char layer, and then only after the char layer has itself cooled. By contrast, the unidirectional pyrolysis wave is not self contained: it always has edges that are in direct contact with the cold surroundings. Those edges provide a much more effective and alternative cooling path that counteracts the char's thermal inertia. Clearly, the unidirectional, laser heated particle can quench more rapidly and thus can freeze or capture the wave and reveal its structure with good spatial resolution. Those structures are clearly seen in figures 15 and 16. For the omnidirectionally heated particle, not only is the wave hidden from view by the enveloping char, but the thermal inertia of the system, and its longer quenching time, will broaden and "blur" the image of the active wave structure even if the particle were sliced or sectioned for inspection.

MACROSCOPIC COAL SAMPLE SEM PHOTOMICROGRAPHS

Experiments were also conducted with macroscopic coal samples heated in the laser beam in order to try to measure the intrinsic thickness of the pyrolysis wave front. The resultant SEM photomicrographs for a sample of Pittsburgh seam bituminous coal are reproduced in figure 17. The sample was cleaved from a larger block of coal. Its approximate dimensions are sketched in the insert at the top of figure 17. Its orientation during laser exposure is also indicated in the insert. The bedding planes were horizontal and the laser beam was incident vertically from above such that the propagation direction of the laser beam was perpendicular to the bedding planes. The sample was exposed to an input laser flux of 100 to 125 W/cm^2 for about 2 s, which caused substantial coking of the surface and its upward expansion and swelling as the char layer built up.

The cleaved face that was viewed by the SEM is indicated in the sketch. The devolatilization wave propagated downward from the laser-heated surface across the bedding planes in the same direction as the laser heating flux vector. The face to be inspected by the SEM was purposefully cleaved before the exposure so that it would be about 20° to 30° beyond the vertical. That was done so that the upper, irradiated surface formed an overhanging cliff which shielded the cleaved face from the incident laser beam. That cleaved face was thus in the shadow of the upper surface and could not be directly heated by the incident laser flux. Thus, only the morphological changes associated with the downward propagation of the pyrolysis

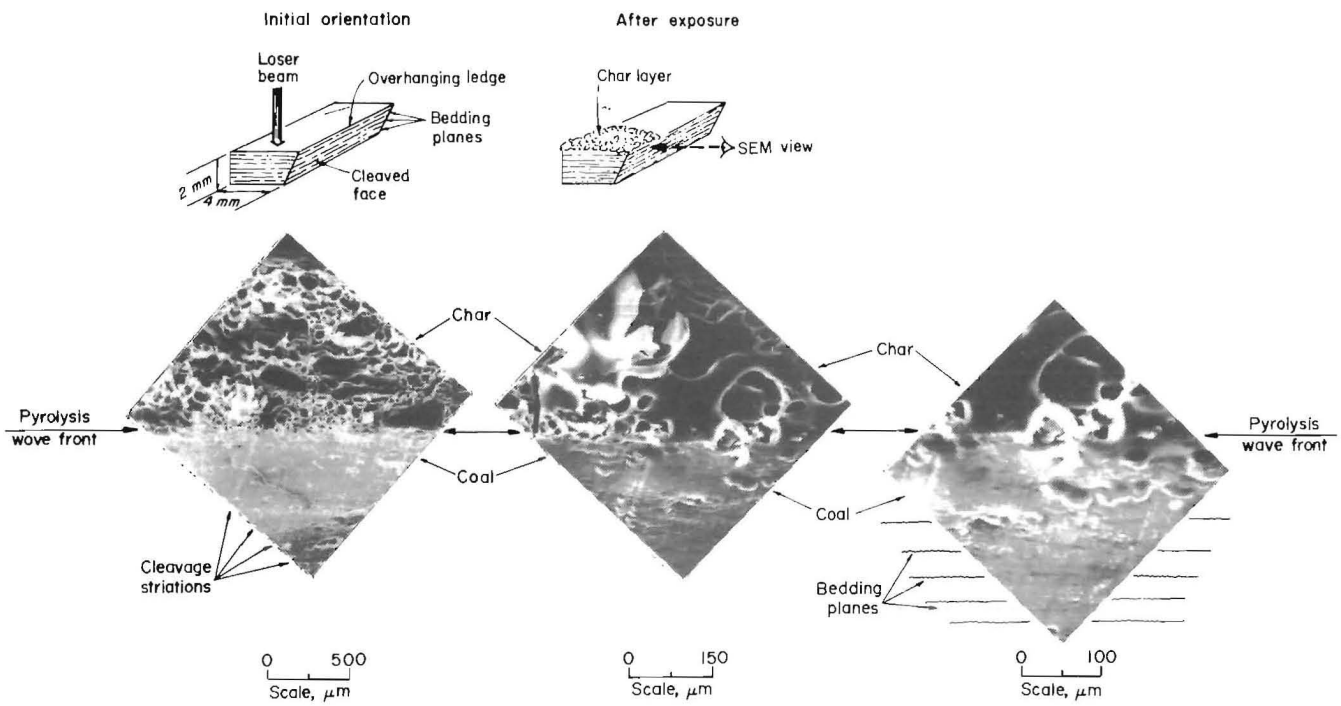

Figure 17.—SEM photomicrographs viewed from the side of a shadowed, cleaved face of a macroscopic sample of Pittsburgh seam bituminous coal exposed for 2 s to a laser flux of 100 to 125 W/cm^2. Pyrolysis and devolatilization wave front is viewed at three magnifications.

wave would be viewed. It was only the edge of the pyrolysis wave that would move down that cleaved face and be viewed by the SEM, as illustrated in the sketch. After exposure, the sample was turned 90° so that the cleaved face or ledge could be analyzed from above by the electron beam of the SEM.

The SEM photomicrographs of the transition region between the char and the unreacted coal are shown in figure 17. The SEM view on the left is a low magnification view of the cleaved face which reveals a rather sharp transition between the porous char above and the undisturbed coal below. The mechanical grooves or striations left by the cleaving knife edge are indicated, and they run perpendicular to the bedding planes. Those striations are clearly not naturally occuring since the grooves are all artificially straight and parallel. In that low magnification view, the transition region between the devolatilized char above and the unreacted coal below appears to be quite sharp. A higher magnification view of the transition region is shown in the SEM photomicrograph in the center of figure 17. A still higher magnification view is shown on the right. The horizontal orientations of the bedding planes are indicated there and they reveal a natural or wavy structure associated with their compaction in geologic time. Even at that higher magnification, it is difficult to estimate the width of the transition zone between the char and the unreacted coal. The cleaved edge is being viewed at an angle of 20° to 30° sloping away from the observer. In addition, the swelling and frothing of the char structure has created an additional overhang which partially obscures one's view of the unreacted coal surface, especially of the transition region. In addition, the pyrolysis wave front itself appears to be as wavy as the bedding planes themselves. Despite those complications, the SEM photomicrographs suggest a reaction zone thickness for the quenched pyrolysis wave that is no larger than about 50 μm. *Thus the wave thickness at 100 to 125 W/cm^2 is about the same for the macroscopic samples of coal as it was for the 200- to 300-μm diameter particles.*

In addition, it should be noted that some of the protruding edges of the bedding planes seem to overhang much more than they should for a mechanically cleaved face. Those exaggerated protrusions are probably caused by accretions of accumulating tars that preferentially recondensed on the cold, protruding edges.

During laser pyrolysis exposure, there is a frothing and upward expansion of bubbling bitumen which generates the low-density char layer once the heavier molecular weight constituents finally solidify in the bubble walls. For the Pittsburgh seam bituminous coal, which has a high swelling index, that density of that bubbling bitumen probably corresponds to the minimum value of 0.2 g/cm^3 observed by Lee, Singer, and Chaiken (*1*) in the region immediately above the unreacted coal surface (see figure 2). The original coal loses about 36 pct of its mass as volatiles, which means that the residue would have a density of 0.85 g/cm^3 if there were no expansion of the structure. The measured minimum density of 0.20 thus corresponds to a volumetric swelling of a factor of 4 to 5 for the char residue. Such a swelling ratio is consistent with the observed bubble density for the Pittsburgh seam char residue shown in figure 17. That swelling is also readily observed visually with the unaided eye as the exposed surface charifies and expands upward. The process leaves a char residue that has very little mechanical strength relative to the coal substrate. The char layer readily flakes off and crumbles even with the mildest of external manipulations after exposure.

The density profiles of Lee, Singer, and Chaiken also reveal a consolidated char layer of higher density that appears above the minimum density zone, but only after longer time exposures in the range of minutes. That more dense, consolidated char with a mass density of 0.8 g/cm^3 is probably formed by two processes: first the compaction and accretion of the frothing and bubbling liquid that subsequently solidifies after it is transported to the very high temperature char layer accumulated at the top surface, and secondly, the cracking of volatiles diffusing through that thickening and hot char layer. That more dense char forms a surface cap only after long exposure times of minutes at their lower fluxes and their low mass flow rate of volatiles. For the high flux exposures on the time scale of a second or two with the rapid flow of volatiles from the surface, there is little opportunity for such a consolidated, dense char cap to form.

In view of the complexities associated with the structural fragility of the char layer formed from the swelling and coking of the Pittsburgh bituminous seam coal during its pyrolysis and devolatilization, it was decided that a noncoking coal should also be investigated. A macroscopic sample of a Wyoming subbituminous (Hannah seam, high volatile C) coal with a low swelling index was chosen. The Hannah coal from the No. 80 seam had a moisture content of 11 pct, an ash content of 5 pct, a volatile matter content of 40 pct, and a fixed carbon content of 44 pct. Its as-received heating value was 11,350 BTU/lb. It is classified as a high volatile C bituminous coal, but, it is clearly on the borderline between bituminous and subbituminous coals. For the purposes of this study, it was chosen because of its low free-swelling index which was 0.5.

A sample of that subbituminous coal was cleaved and exposed to a laser flux of 100 to 125 W/cm^2 for 1 s. The sample configuration, relative to the laser beam, was similar to that sketched previously in figure 17. For the Wyoming coal, the bedding planes were also oriented horizontally and the laser beam was also incident from above. For the Wyoming coal, the bedding planes are not as readily discernable as they were for the Pittsburgh seam coal. For the Wyoming coal, well developed orthogonal fracture patterns appear both parallel to and perpendicular to those bedding planes. The resultant SEM photomicrographs of the edge of Wyoming coal sample are shown in figure 18. The position of the pyrolysis and devolatilization wave is clearly visible and is indicated. The char layer above the pyrolysis wave front appears more dense and consolidated. Only an occasional, small blowhole is visible on the surface of the Wyoming char in contrast to the Pittsburgh seam bituminous char residue whose surface consisted mostly of blowholes. The Wyoming coal char structure, seen in figure 18, is so well consolidated that it contains a clear imprint or structural record of the previous positions of the pyrolysis wave front. There are ridges of previously resolidified bitumen that run parallel to the bedding planes. Those ridges are clearly visible in the char layer above and they outline the wavy structure of the naturally occurring bedding planes. Those ridges are the charified residue of liquid bitumen that had been oozing out from between those bedding planes as the pyrolysis wave front passed through. When the bitumen resolidified into a char in the wake of the wave it left its imprint in the form of a series of ridges that run parallel to the bedding planes.

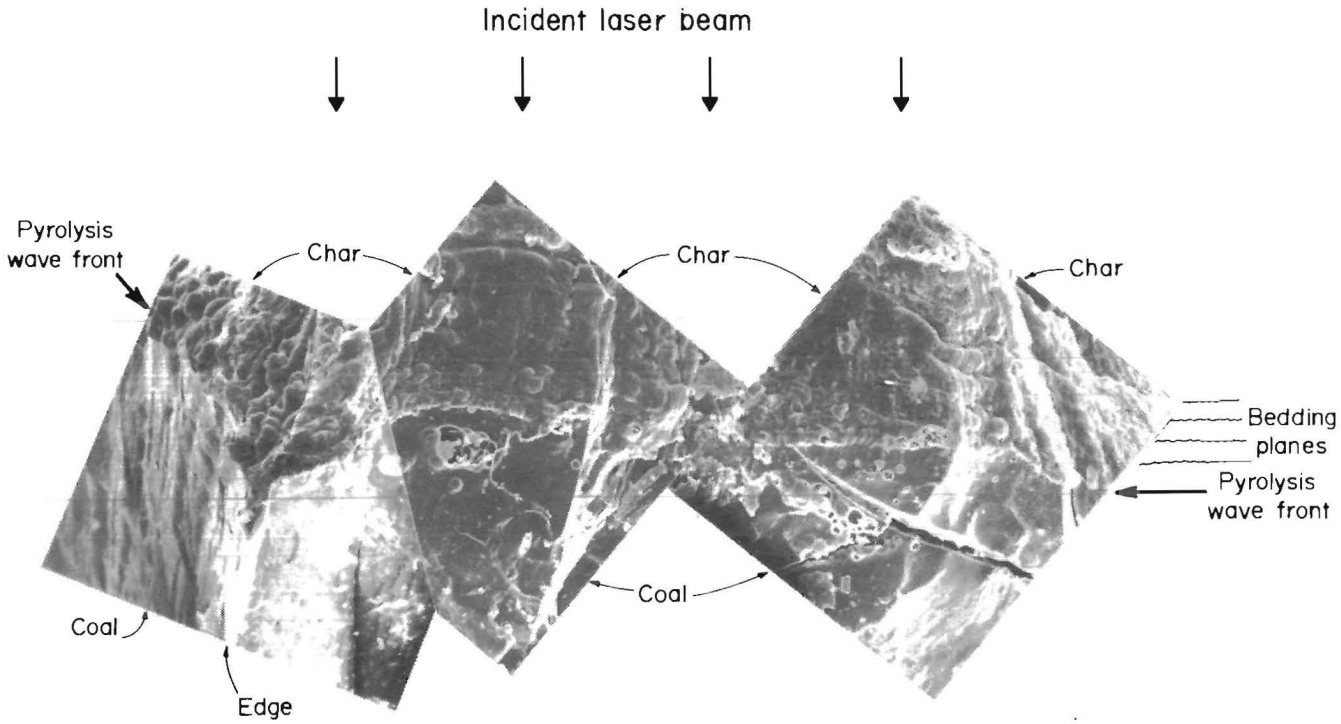

Figure 18.—SEM photomicrographs, viewed from the side of a macroscopic sample of a low-swelling-index, Hannah-seam, Wyoming coal exposed for 1 s to a laser flux of 100 to 125 W/cm^2.

The undisturbed coal surface is clearly seen below the pyrolysis wave front with its angular cracks and sharply cleaved faces and corners. There is an occasional bubbled patch or region at the surface of the unreacted coal below the pyrolysis zone that should be ignored. In this case, the coal surface below was not completely shadowed by an overhanging cliff. The occasional patches of char are the remains of small horizontal protrusions that were in the direct path of the laser beam and were burned off. But, most of the coal surface that is seen below the wave front was clearly in the shadow of the irradiated upper surface and shows no evidence of any pyrolysis or devolatilization. Toward the lower left of the montage of SEM photomicrographs is a sharp right-angle corner or edge. The outline of the pyrolysis wave front can be readily seen as it turns that corner although it is obscured somewhat by the overhanging char ridges.

Another macroscopic sample of the Wyoming subbituminous coal is shown in figure 19. The tall, thin sample, 6 by 1 mm in cross section, was exposed to the laser flux of 100 to 125 W/cm^2. The left side of the sample was oriented in the center of the beam, whereas the right side of the sample was just at the boundary of the beam. The laser flux on the left side of the sample was clearly larger than on the right side. As a result, the pyrolysis wave front progressed some 1,000 μm (1 mm) into the sample on the left side, whereas on the right side the wave progressed only about 200 μm during the same 2–s exposure time.

A low magnification view of the side of the exposed sample is shown in figure 20, which is a montage obtained from several overlapping SEM photomicrographs. The pyrolysis wave front whose position was frozen when the laser beam was turned off after the 2–s exposure, is clearly visible. The pyrolysis front runs mainly horizontally through the sample, and the thermal gradient associated with its propagation has induced mechanical stresses which caused substantial cracking. The surface of the char residue above the pyrolysis wave front contains some blowholes, but the surface density of blowholes in this lower rank, Wyoming coal is clearly less numerous than for the higher rank Pittsburgh coal in figure 17. There is less swelling and expansion of the char for this lower rank coal, but that swelling is nevertheless observable as a persistent overhang or bulging out of the char structure just above the pyrolysis zone, as can be seen in figure 20, and the higher magnification views shown in the lower part of figure 19.

Those higher magnification views are reproduced in figures 20 through 25, and they reveal in more detail the structure of the pyrolysis zone transition between the char structure above and the coal structure below. The mechanical stresses induced by the temperature gradient under laser heating has resulted in substantial fracturing during the pyrolysis and char formation process. Since the most significant thermal expansion process occurs during pyrolysis and devolatilization, the greatest stresses are in the transition or pyrolysis zone between the coal and the char. The fracture pattern is an orthogonal one which tends to align itself with the pyrolysis wave front. The lower rank coal is less plastic and hence the cracking pattern is more extensive. There were clearly preexisting stress patterns in the original coal sample and they reveal a somewhat independent orthogonal fracture pattern associated with the bedding plane orientation. The interaction of those two stress patterns—the original one and the one induced by devolatilization—provides the observer with a revealing, in-depth view of the pyrolysis zone, as can be seen in figures 21 through 24.

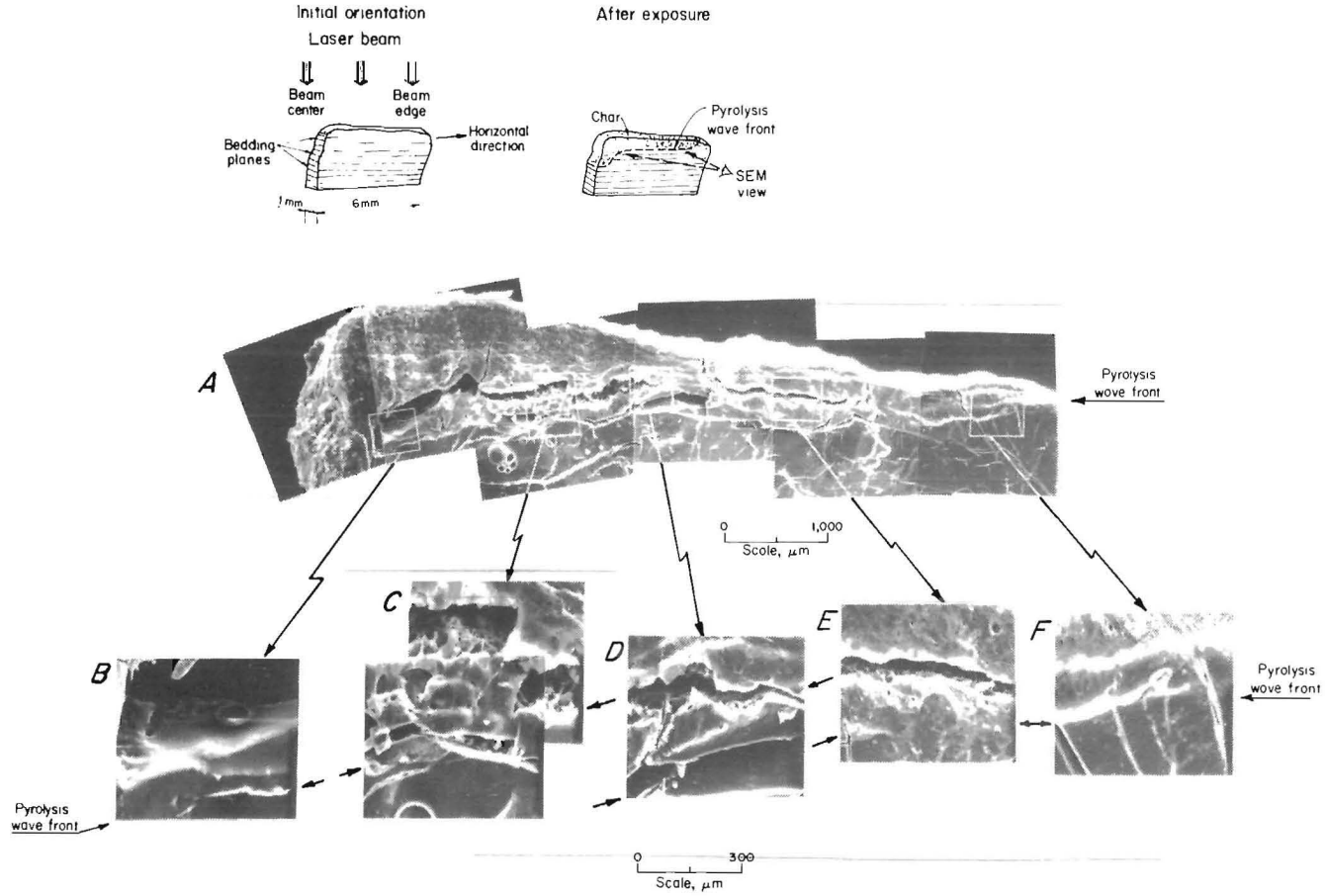

Figure 19.—SEM photomicrographs of a macroscopic sample of Hannah-seam coal exposed to a maximum laser flux of 100 to 125 W/cm^2 for 2 s, as viewed from the side. Lower magnification montage in *A*; higher magnification views of the pyrolysis and devolatilization wave front in *B*, *C*, *D*, *E*, and *F*.

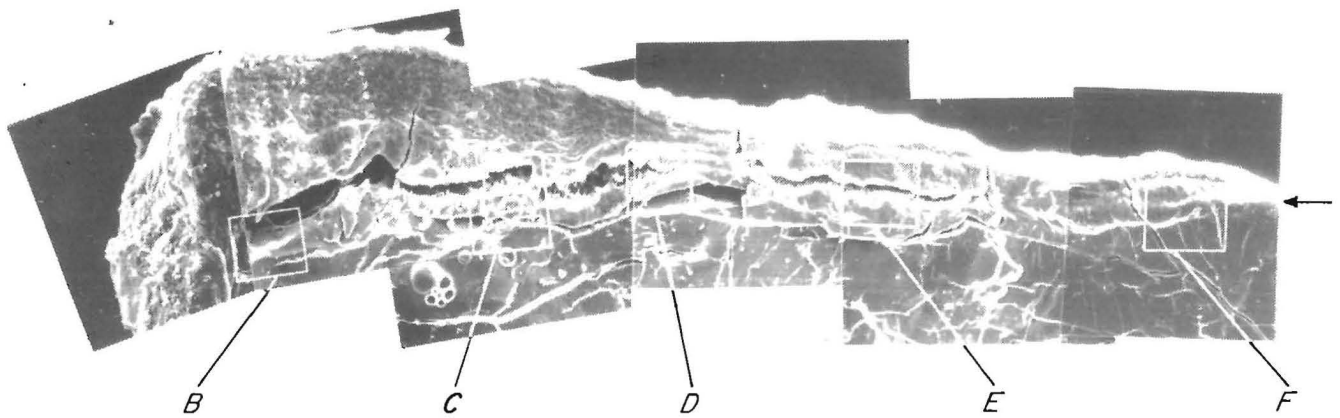

Figure 20.—Montage *A* (fig. 19) magnified to provide more detail. Arrow indicates position of the pyrolysis wave front.

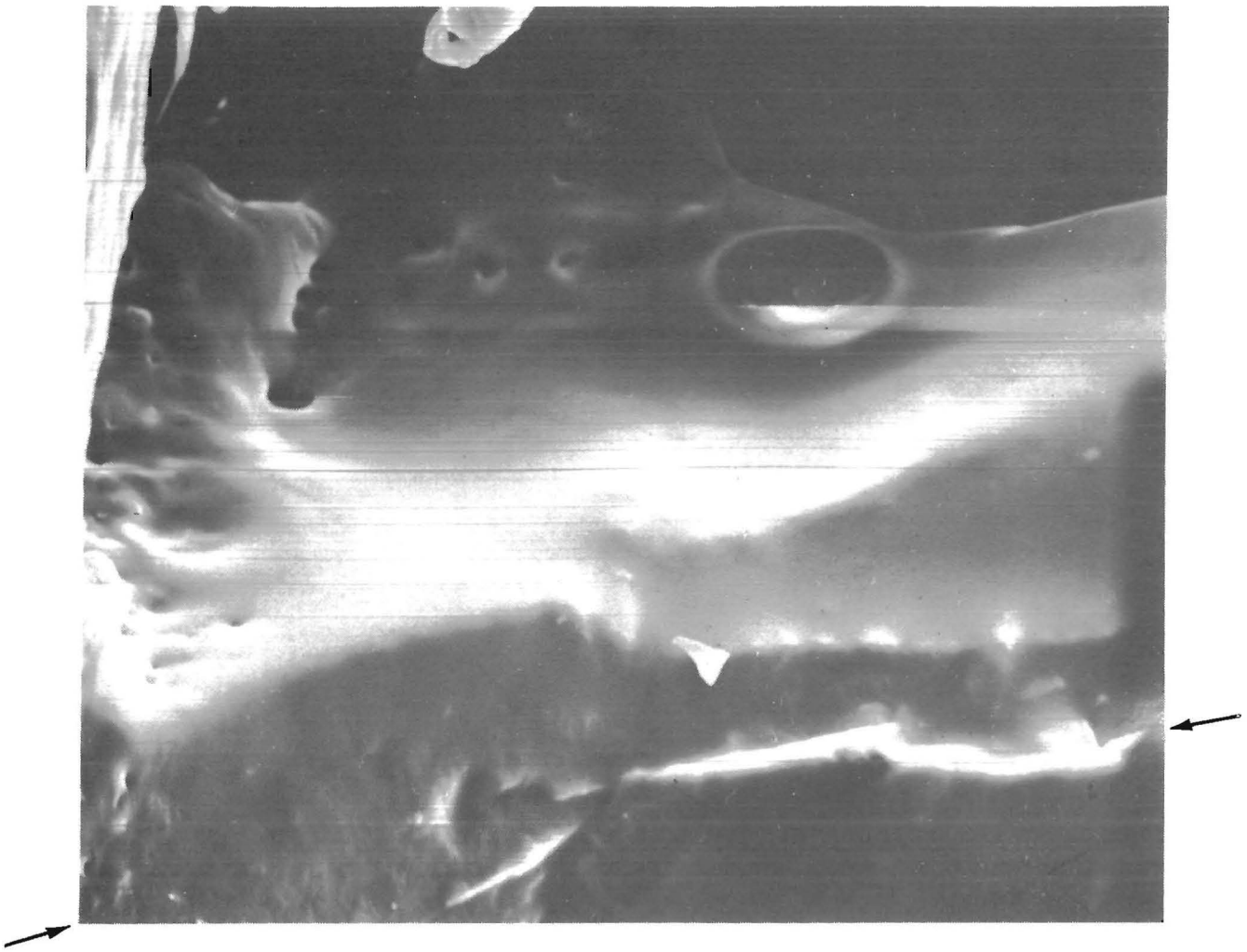

Figure 21.—Section *B* (fig. 19) magnified to show more detail. Arrows indicate position of pyrolysis wave front.

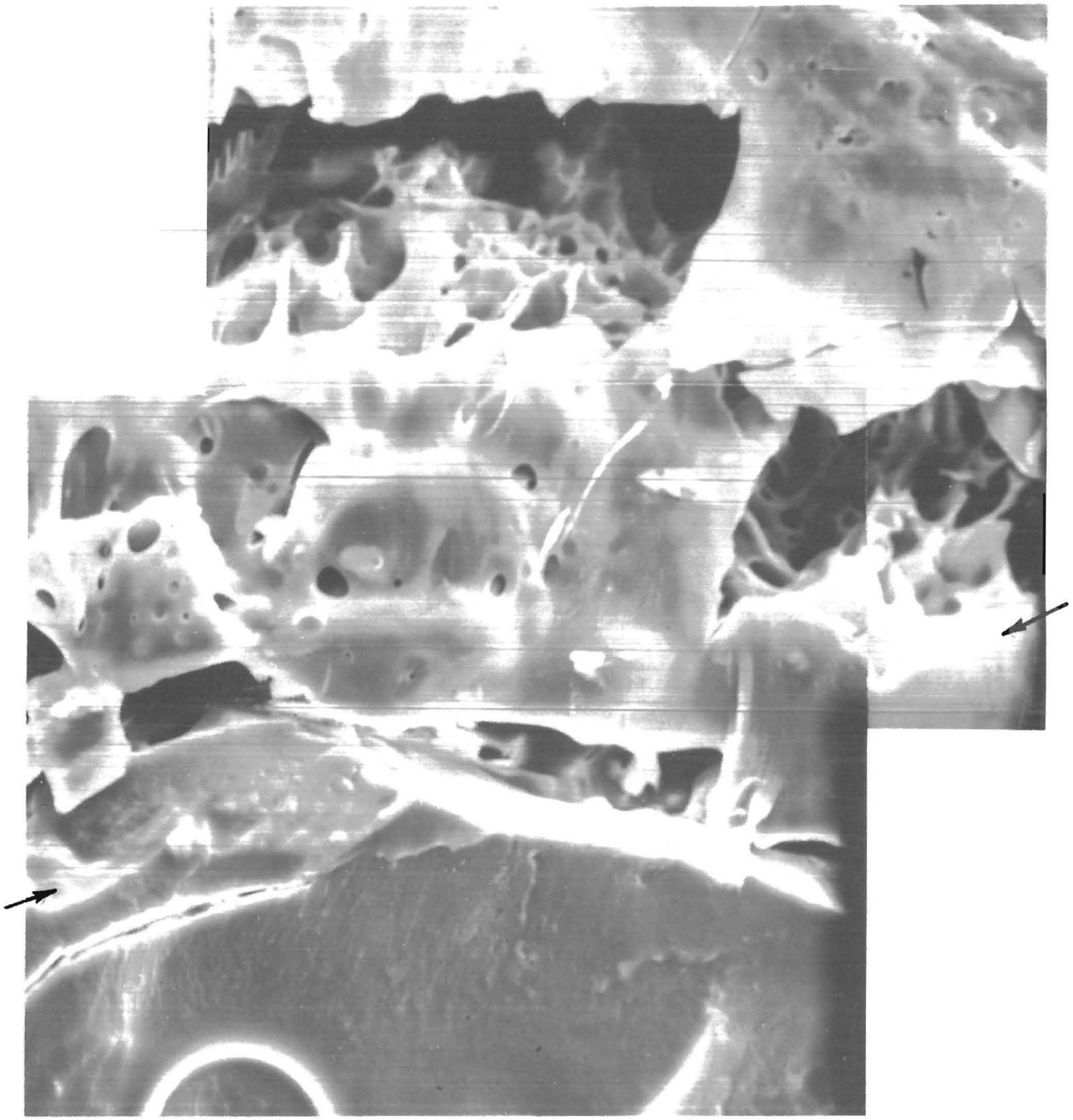

Figure 22.—Section *C* (fig. 19) composite magnified to show more detail. Arrows indicate position of pyrolysis wave front.

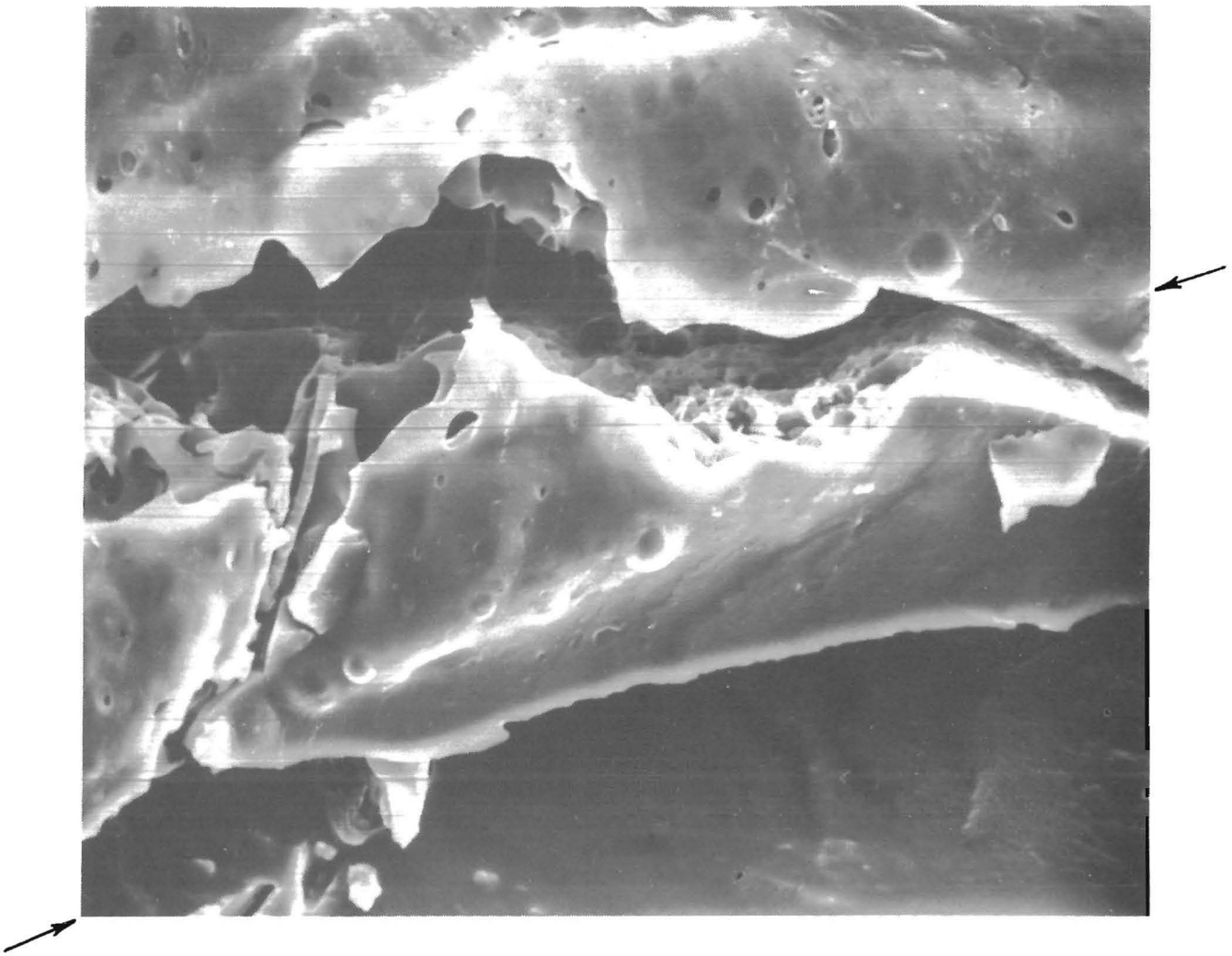

Figure 23.—Section *D* (fig. 19) magnified to show more detail. Arrows indicate position of pyrolysis wave front.

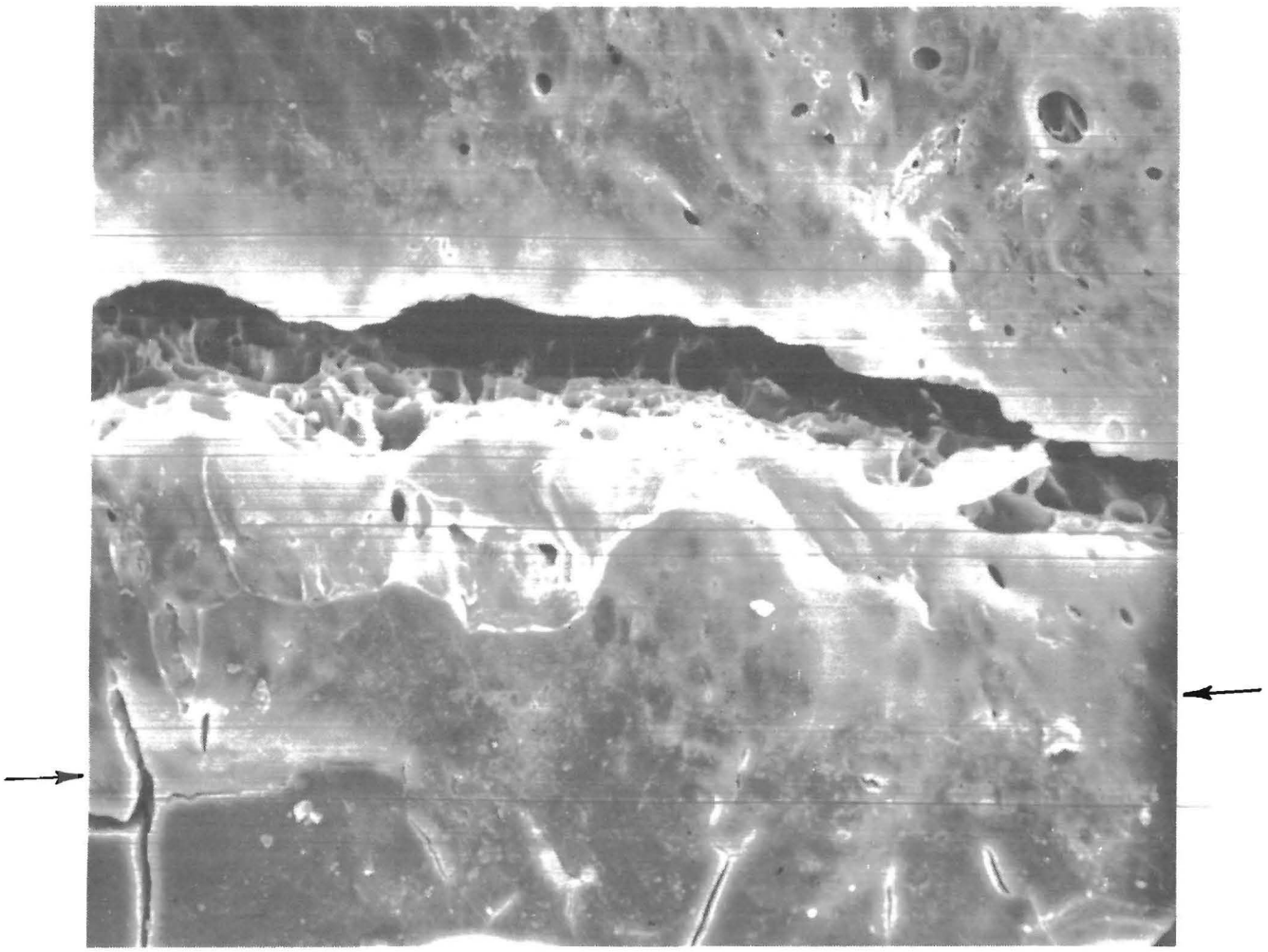

Figure 24.—Section *E* (fig. 19) magnified to show more detail. Arrows indicate position of pyrolysis wave front.

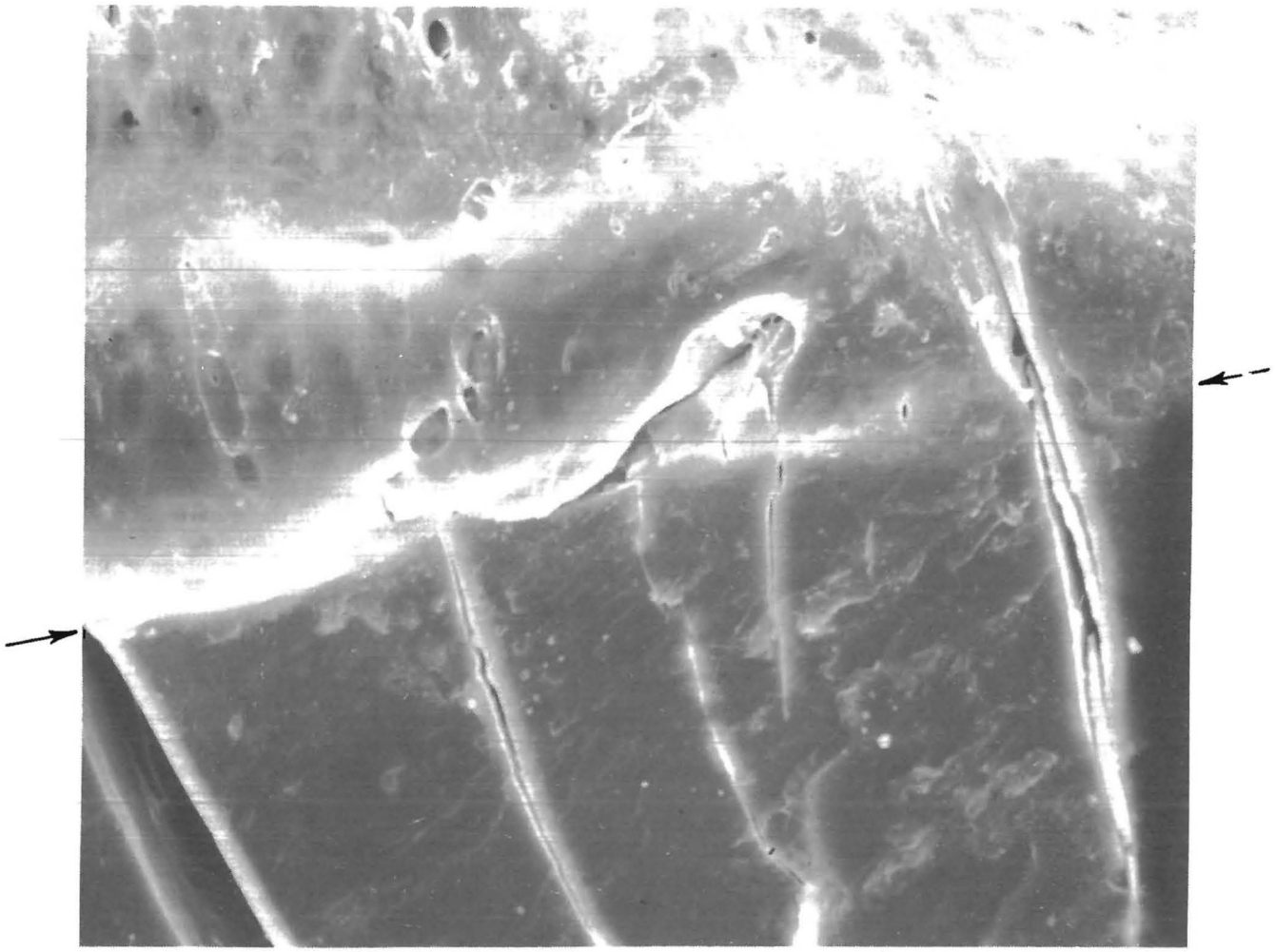

Figure 25.—Section *F* (fig. 19) magnified to show more detail. Arrows indicate position of pyrolysis wave front.

It is instructive to systematically consider each of the higher magnification SEM photomicrographs of the pyrolysis zone. The consideration will start on the right of the sample and move from right to left. The lowest flux exposure is seen in figure 25 and the position of the pyrolysis wave front is clearly revealed there by the bulge or overhang of the expanding char layer, which is located just above the unreacted coal. In figure 25, one sees a series of parallel, vertical, preexisting fracture cracks located in the original coal structure just below the pyrolysis wave front. The SEM photomicrograph clearly reveals that the narrower fracture cracks are being sealed or healed as the partially molten pyrolysis wave front propagates along their length. On the outside surface of the char, the density of blowholes is relatively low and from that view alone one might infer that the char is relatively dense; however, the in-depth views of that char structure, which will be seen shortly, reveal otherwise.

In figure 24, the SEM has focused on a horizontal crack in a large section of char that has begun to flake off and separate from the main body of the sample. That horizontal crack is contiguous with two vertical cracks on both sides (center, right in figure 20), and the entire piece of char appears to have been displaced upward by about 60 to 70 μm. That upward displacement or separation reveals an in-depth view of the structure of the char, which is clearly seen in figure 24. That in-depth view of the char structure reveals a honeycombed structure that is much less dense than would be inferred from the small number of blowholes at the char surface. The horizontal crack is entirely within the char layer and it is located near the top of the bulge or overhang. The pyrolysis wave front is located at the bottom of the bulge, some 150 to 200 μm below that large horizontal crack.

In figure 23, the SEM has been focused on two horizontal cracks in the sample. The lower crack is entirely within the undisturbed coal below the pyrolysis zone. The lower face of that lower crack is clearly seen, and it reveals the original coal structure which is smooth and featureless. The upper crack or fissure is much more interesting because it actually intersects the pyrolysis wave front at an angle of about 30°. The lower face of that upper crack thus reveals not only an in-depth view of both the char structure and the coal structure, but it also reveals an in-depth view of the structure of the pyrolysis wave front transition zone. Thus in figure 23, the lower face of the upper fissure reveals the honeycombed char structure toward the left side of the fissure, but a solid coal structure on the right side. The in-depth structure of the transition zone or pyrolysis wave front is again quite sharp. Although its structure may be a bit wavy, the intrinsic width of the transition zone between the honeycombed char and the solid coal is again less than 50 μm. Figure 23 also shows clearly that the overhang or bulge in the surface structure of the char begins precisely at that pyrolysis wave front discontinuity.

Figure 22 also contains two horizontal fractures. The upper fracture runs through the char only and contains an orthogonal step. The lower fracture appears to coincide with the pyrolysis wave front: its lower face consisting of coal and its upper face of char. The surface bubble near the bottom of figure 22 should be ignored. It again represents the remains of a surface protrusion in the side of the sample that was not in the shadow of the exposed top surface. Such protrusions are directly exposed in the laser beam and are rapidly burned off by the laser leaving such small, circular pockmarks in the otherwise undisturbed coal surface. A similar group of isolated bubbles is visible to the left of that bubble in the montage of figure 20. Again those bubbles are the remains of protrusions that were burned away by direct laser exposure and are not representative of the rest of the surface structure of the original coal which was successfully shielded from the laser by the top surface of the sample.

In figure 21, the SEM was focused on the lower face of a fracture crack that was formed very close to the pyrolysis wave front. That lower face appears to have been partially molten before it resolidified. The region being viewed is actually a corner formed by the intersection of two pyrolysis wave fronts: one propagating downward from the upper surface, and another propagating toward the right from the sloping side of the sample. That sloping side is also directly exposed to the laser beam but at an oblique angle.

The SEM photomicrographs in figures 17 through 25 provide direct and undisputable proof that the coal pyrolysis process proceeds via the propagation of a pyrolysis and devolatilization wave front. The intrinsic width of that wave front is less than 50 μm at flux exposures that are comparable to those experienced by coal particles in burner flames.

THEORETICAL DEVELOPMENT

For a more precise theoretical formulation of the problem, one considers a finite length solid extending from its planar surface at $x = 0$ to $x = L$, whose temperature distribution in both space and time are to be determined as that surface is exposed to a laser heating flux, I. Heat transfer is considered only in the axial direction, x. Transverse heat is assumed to be negligible. In general, the temperature field within the solid, $T(x,t)$, will be a function of both distance from the surface, x, as measured in the laboratory coordinate system, and the time of exposure, t.

Initially, before the laser is turned on ($t < 0$), the solid is isothermal and at room temperature, so that $T(x, 0) = T_o$. The laser heating source is turned on at $t = 0$ and the surface of the solid at $x = 0$ is thereafter heated by a constant radiant flux whose plane wave intensity, I, is normal to that surface. Initially, the position of the planar surface remains stationary in the laboratory coordinate system because the surface temperature is too low for vaporization to occur. As time proceeds, the surface temperature, $T(0,t)$, will increase and if it becomes high enough, the solid at the surface will vaporize or sublime.

Such vaporization will cause the surface discontinuity to regress relative to the laboratory observer at a rate, $\dot{x}_o(t)$. In general that regression of the exposed surface is a function of time.

In the laboratory coordinate system, the energy conservation equation for the one dimensional solid that still extends from $x = x_o$ to $x = L$, where x_o is the location of the moving solid boundary, is

$$\rho\, C(T)\, \frac{\partial T}{\partial t} = \frac{\partial}{\partial x}\left[\lambda(T)\, \frac{\partial T}{\partial x}\right]. \qquad (18)$$

The rate of change of the energy content per unit volume of *space* is $\rho\, C(T)\, \frac{\partial T}{\partial t}$. It is determined by the net rate of heat conduction into that space from adjacent volumes, $\frac{\partial}{\partial x}\left[\lambda(T)\, \frac{\partial T}{\partial x}\right]$.

In general, the heat capacity, C(T), and the thermal conductivity, $\lambda(T)$, are both functions of temperature. The solid is assumed to have a low coefficient of thermal expansion so that its density, ρ, is taken to be constant. For the application considered here, λ is also taken to be constant.

Initially, for $t < 0$, the solid is isothermal at $T(x,t) = T_o$ and the heating flux is zero. At $t = 0$ the surface heating flux is turned on and it is maintained at a constant value, I, from $t = 0$ to $t = \infty$. A portion of the incident radiant flux is reflected from the surface and another portion is lost to the surrounding by nonadiabatic loss processes. The net absorbed flux is therefore $I(1-r) - I_\ell$, where r is the reflectance and I_ℓ is the loss flux. It is here assumed that the absorption coefficient of the solid is so high that essentially all of the net absorbed flux is deposited at the planar solid discontinuity, that is, at $x = 0$. The vaporization or sublimation process is here assumed to occur instantaneously as the surface temperature, T(0, t), reaches a threshold vaporization temperature, T_s. If T(0, t) is below T_s, no vaporization can occur and $\dot{x}_o = 0$. For those assumptions the energy flux balance at the boundary, $x = 0$, is given by

$$I(1-r) - I_\ell = \lambda(T_s)\left(\frac{\partial T}{\partial x}\right)_o + \rho\, \dot{x}_o(t)\, \Delta H_v. \qquad (19)$$

The net absorbed flux at the boundary is partitioned into a heat flux conducted into the colder solid, $\lambda(T_s)\left(\frac{\partial T}{\partial x}\right)_o$, and a heat flux of vaporization, $\rho\, \dot{x}_o(t)\, \Delta H_v$. Although vapors are emitted from the surface and they transport mass away from the boundary, those vapors are emitted at the surface vaporization temperature, T_s. Equation 19 is therefore a boundary constraint at the discontinuity $x = 0$. The other constraint at the moving surface is that the surface temperature, T(0,t), cannot exceed the vaporization temperature, T_s.

The geometric boundary of the solid at $x = L$ is in contact with an adiabatic surface. That adiabatic boundary condition at a distance far from the surface is most simply attained by the condition that

$$\frac{\partial T}{\partial x} = 0 \text{ at } x = L. \qquad (20)$$

The problem defined by equations 18 through 20 is similar to the ablation problem modeled by Zien (*33*), who considered a semi-infinite solid.

NON-STEADY-STATE INDUCTION TIME

The solution to equation 18 with the boundary constraint of equations 19 and 20 as well as the other assumptions indicated, may be resolved into two time periods. During the early time period there is only an initial heating near the surface in which the surface temperature rises from T_o toward the vaporization temperature, T_s. A subsurface temperature profile is also developed during that early time period as the absorbed flux is conducted inward. But so long as the surface temperature remains below T_s, there is no vaporization and $\dot{x}_o = 0$. Thus there is a period of time between $t = 0$ and $t = \tau$, for which T(0, t) is less than T_s, during which there is no regression of the surface. The time, τ, required for the surface to reach that vaporization temperature is here referred to as the induction time.

During the induction period, equation 18 can be solved analytically if the heat capacity is assumed constant and the finite length solid is approximated as a semi-infinite solid. The assumption of representing a 1-cm length of polymethylmethacrylate (PMMA) by a semi-infinite solid was validated in a numerical study that is discussed later. The analytical solution is given in Carslaw and Jaeger (*34*):

$$T(0,t) - T_o = 2[I(1-r) - I_\ell]\, [t/\pi C\rho\lambda]^{1/2}. \qquad (21)$$

The time required for the surface to reach T_s is the induction time, τ, and it is therefore given by

$$\tau = \frac{\pi}{4}\, C\rho\lambda\, (T_s - T_o)^2/[I(1-r) - I_\ell]^2. \qquad (22)$$

Equation 22 may be applied directly to the case of PMMA for which the data were presented in figures 12 and 13. The measured induction times were also summarized in table 1. One may therefore compare the measured τ values with those predicted by equation 22. For PMMA the devolatilization surface temperature is again taken as 400° C so that $T_s - T_o = 400°\text{ C} - 25°\text{ C} = 375°\text{ C}$. The average heat capacity between 25° and 400° C is obtained as before (*28*), and is 0.52 cal/(g·°C). The thermal conductivity for PMMA (*29*) is taken as 4.5×10^{-4} cal/(cm·s·°C). The solid density is 1.18 g/cm^3. Substituting into equation 22 yields

$$\tau(s) = 534/[I(1-r) - I_\ell]^2, \qquad (23)$$

where the absorbed flux is expressed in watts per square centimeter. In table 2, the induction times calculated from equation 23 are compared with the data previously summarized in table 1.

The comparison of the measure τ values with those predicted by equation 23 shows good agreement for the higher incident fluxes. For the lower incident fluxes, equation 23 as is, predicts substantially longer induction times than those measured experimentally. It should be noted however, that at those lower flux values, the loss flux used ($I_\ell = 9.8$ W/cm^2) is a major fraction of the incident flux, I. Actually that loss flux was inferred from the steady-state data shown in figure 13. For that steady-state case the surface temperature has already reached T_s.

Table 2.—Comparison of measured induction time for laser pyrolysis of PMMA with theoretical calculations

Flux, W/cm^2		Induction time (τ), s			
			Calculated		
Incident (I)	Net [I(1 − r) − I_ℓ]	Measured	eq. 23, steady state (I_ℓ)	eq. 23, with I_ℓ = 0	Variable C(T) steady state (I_ℓ)
115	97.2	0.101	0.057	0.047	NA
70.7	56.2	.160	.169	.123	0.04
42.5	29.7	.50	.605	.342	.57
23.2	11.8	1.83	3.84	1.16	3.9
12.4	1.73	6.7	178	4.04	NA

NA Not available.

During most of the induction period, however, the system is not in steady state, the surface temperature is well below T_s, and the loss flux is substantially lower than the value inferred from the steady-state data. Clearly during the induction time, I_ℓ is time dependent. It will be quite low initially while the sample is at ambient temperature, and will approach the steady-state value of 9.8 W/cm^2 only as the surface temperatures approaches T_s. That occurs only later in the induction period. In order to estimate the magnitude of the effect of such a time-dependent loss flux, $I_\ell(t)$, which is initially near zero, the induction time was also calculated from equation 23 for the other extreme case in which $I_\ell = 0$.

For high incident fluxes where $I_\ell << I$, the effect of setting $I_\ell = 0$ is small; however at the lower fluxes where $I_\ell \rightarrow I$, the effect is very significant, and the predictions with $I_\ell = 0$ give better agreement with the data. Clearly the average loss flux during the induction period is realistically much smaller than the steady-state value of I_ℓ. With the extreme assumption that $I_\ell = 0$, the calculated τ values are lower than the measured ones. Clearly the real, time average losses, $I_\ell(t)$, are intermediate between the two extremes of 0 and 9.8 W/cm^2, but closer to the former.

The solution to equations 18 and 19 that is given by equation 22 assumes that the heat capacity, C(T), is constant. Numerical solutions of equation 18 and 19 were also obtained for a variable heat capacity and those results are also shown in table 2 for the case in which I_ℓ = 9.8 W/cm^2. The variable heat capacity was taken as a linearized version of the Bares and Wunderlich data (*28*), and was represented by the equation: C(T) = 0.042 + 0.975 x 10^{-3} T. The best agreement between measured and predicted induction times occurred at the intermediate flux of 42.5 W/cm^2 for the variable heat capacity model. Again a more realistic model should also include a time-dependent heat loss flux from the sample.

The comparison of the variable heat capacity calculations with those of a constant, average heat capacity suggests that the use of an average value for C(T) is sufficiently accurate for low incident fluxes. The major uncertainty in predicting τ comes from the variable loss flux, I_ℓ (t).

In addition, the comparison of the measured τ values with all of the predictions suggests that measured flux dependence is milder than the predicted inverse square dependence of equation 23. The flux levels in table 2 vary by an order of magnitude and hence the predicted τ values are varying by two orders of magnitude. Yet the measured τ values are showing a milder flux dependence. That difference is attributed to the theoretical assumption that the input flux is absorbed entirely at the surface. In reality, the energy is absorbed somewhat in depth, which gives a somewhat broader temperature profile, which should moderate the predicted inverse square flux dependence.

TRANSIENT SOLUTION

The energy transport equation, equation 18, and the associated boundary conditions, equations 19 and 20, as applied to a finite length sample of PMMA with a temperature-dependent heat capacity, defines a nonlinear model of vaporization (sublimation). A solution to the partial differential equation, equation 18, defines the localized time-dependent solid temperature. The progression of the isotherm defined by T_s through the solid defines the regression of the boundary surface, x_o. The complexity of the model equations requires a numerical solution. This was accomplished through a finite difference representation of the partial derivatives that used central differencing for the spatial second partial derivative in equation 18, and forward differencing for the first partial derivatives in equation 19 and 20. Forward time differencing was used for the partial derivative with respect to time in equation 18. The finite difference equations were written implicit in time, and were in tridiagonal form with respect to the space variables.

This representation is readily solved with application of the Thomas algorithm (*35*). The numerical scheme was developed into a FORTRAN computer program that could be used for user prescribed values of thermal properties, sample length, and net incident flux. The program output included the temperature throughout the solid at specified times, as well as the location of the moving surface. For these calculations a 1-cm-length sample was considered. Temperature evaluations were made at locations separated by 10^{-3} cm throughout the sample.

The model equations are applicable to a temperature that changes in a continuous manner with respect to space and time. To accommodate the continuity of the temperature, it was computationally necessary to represent the endothermic heat of pyrolysis by a continuous function of temperature, $\Delta H(T)$:

$$\Delta H(T) = \Delta H_v/(1 + e^{-(T^* - T_s)}).$$

This equation mathematically smooths the transition from a nonpyrolyzing state during the induction period to a pyrolyzing state following the induction period. The temperature, T*, is the instantaneous temperature of the moving boundary surface.

The discrete representation of the continuous heat transport process by the finite difference equations can

result in a surface temperature slightly greater than the pyrolysis temperature, T_s. The preceding equation assures that the pyrolysis is 99 pct effective if T* exceeds T_s by more than 5 K.

A set of computations were made for fluxes of 23.0, 42.5, and 71 W/cm^2 incident upon a 1-cm-long PMMA sample. Figure 26 shows the predicted and measured values of the time-dependent mass loss. Agreement between predicted and measured values is very good at the high flux, and poor at the low flux. The source of the error resides in the use of a flux independent energy loss. In particular, a low incident radiant flux will result in a less rapid rate of change in that loss flux than will a high incident flux.

STEADY-STATE SOLUTION

As time proceeds, and for exposure times that are longer than the induction time, the surface temperature is maintained at T_s and a steady-state subsurface temperature profile is developed. The devolatilization rate becomes steady and constant in time at some constant value, $\dot{x}_o$. In order to obtain a steady-state solution to the problem, it is necessary to consider the conservation equation in a coordinate system that is regressing at that constant velocity, $\dot{x}_o$. In that coordinate system, the planar discontinuity is maintained at x = 0 since the energy conservation equation is considered in a coordinate system that is moving at $\dot{x}_o$ relative to the laboratory observer.

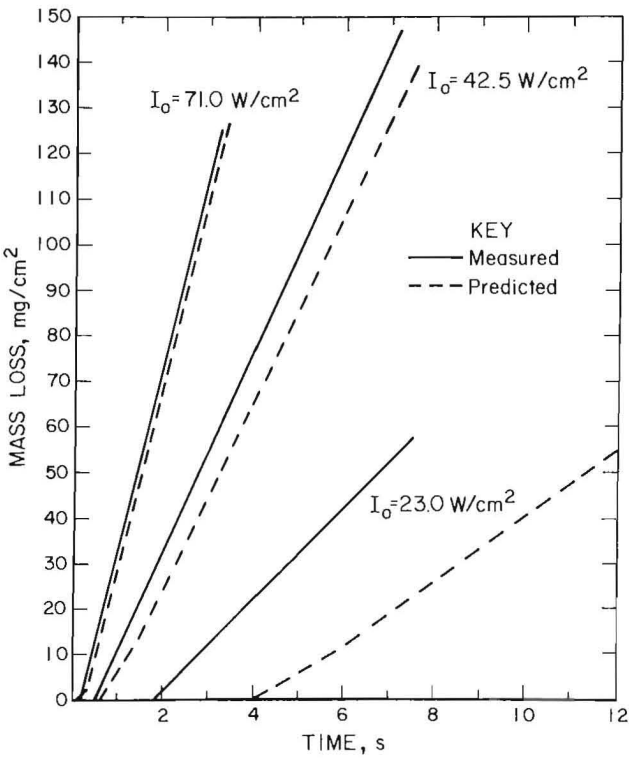

Figure 26.—Measured and predicted weight loss for PMMA for incident fluxes of 71, 42.5, and 23 W/cm^2.

In that coordinate system, the energy conservation equation for the semi-infinite solid, which still extends from x = 0 to x = ∞, becomes

$$\rho\, C(T)\, \frac{\partial T}{\partial t} = \frac{\partial}{\partial x}\left[\lambda(T)\, \frac{\partial T}{\partial x}\right] - \rho\, \dot{x}_o(t)\, C(t)\, \frac{\partial T}{\partial x} \quad . \qquad (24)$$

The rate of change of the energy content per unit volume of *space* is $\rho\, C(T)\, \frac{\partial T}{\partial t}$. It is determined by the sum of the rate of heat conduction into that space from adjacent volumes, $\frac{\partial}{\partial x}\left[\lambda(T)\, \frac{\partial T}{\partial x}\right]$, and the rate of convective transport of heat into that space from adjacent volumes, $-\rho\, \dot{x}_o(t)\, C(T)\, \frac{\partial T}{\partial x}$. Although the medium being considered is a solid in which there is no relative motion of one region of the solid with respect to any other region, mass is nevertheless being convected into each unit volume of space at the velocity, $\dot{x}_o(t)$, by virtue of the motion of the coordinate system. That motion is required in order to maintain the heated surface at x = 0.

The steady-state solution to the problem is obtained by setting $\frac{\partial T}{\partial t} = 0$ in equation 24 and the resultant partial differential steady-state energy conservation equation becomes an ordinary differential equation with only one variable, x:

$$\frac{d}{dx}\left[\lambda(T)\, \frac{\partial T}{\partial x}\right] = \rho\, \dot{x}_o\, C(T) \frac{dT}{dx} \quad . \qquad (25)$$

In steady-state, the rate of heat conduction into any volume of space is balanced by the convective transport out of that volume. If one integrates the left-hand side of the equation with respect to distance x, one has an exact differential for the variable, $\lambda(T)\frac{dT}{dx}$, which is directly integrable from the surface at x = 0 to its infinite boundary at x = ∞. Thus

$$\int_{x=\infty}^{x=0} \frac{d}{dx}\left[\lambda(T)\frac{dT}{dx}\right] dx = \int_{\lambda(T_o)\,(\frac{dT}{dx})_\infty = 0}^{\lambda(T_s)\,(\frac{dT}{dx})_o} d\left[\lambda(T)\, \frac{dT}{dx}\right] = \lambda(T_s)\,(\frac{\partial T}{\partial x})_o. \qquad (26)$$

Whatever the solution may be to the steady-state temperature, T(x), it is a monotonic and single-valued function of x. As a result, the variables λ(T) and C(T) may be expressed either as functions of T or of x. Spatial integrals are thus readily and uniquely transformable into temperature integrals. The right-hand side of equation 25 may be similarly integrated with respect to x, and may then be transformed into an equivalent temperature integral, as follows:

$$\int_{x=\infty}^{x=0} \rho\, \dot{x}_o\, C(T)\, \frac{dT}{dx}\, dx = \rho\, \dot{x}_o \int_{x=\infty}^{x=0} C(T)dT = \rho\, \dot{x}_o \int_{T_o}^{T_s} C(T)dT. \qquad (27)$$

Equating 26 and 27, which were the left- and right-hand sides of equation 25, gives the integrated form of the steady-state energy conservation equation:

$$\lambda(T_s)\left(\frac{dT}{dx}\right)_o = \rho\,\dot{x}_o \int_{T_o}^{T_s} C(T)\,dT. \qquad (28)$$

Substituting equation 28 into equation 19 gives

$$I(1-r) - I_\ell = \rho\,\dot{x}_o \left[\int_{T_o}^{T_s} C(T)\,dT + \Delta H_v\right], \qquad (29)$$

which is identical to equation 7. It is the energy conservation equation for the system in integral form. It simply states that in order for the system to sustain the steady-state mass vaporization rate of $\dot{x}_o\,\rho$, the absorbed energy flux must be sufficient to first raise the temperature of each element of the solid from T_o to T_s, and secondly to supply the heat of vaporization as it devolatilizes. The validity of equation 29 has been amply demonstrated by the data presented earlier.

SUMMARY AND CONCLUSIONS

This report has presented a detailed evaluation and analysis of a diverse set of measurements by many investigators related to the mechanism of pyrolysis and devolatilization of coal and polymethylmethacrylate (PMMA). The observations include data on the rates of pyrolysis and devolatilization, the thermal structure of the reacting system, and SEM photomicrographs of the morphological structural changes that occur during those processes. The specific data that were presented and analyzed were—

1. The mass loss rates, temperature structure, and density profiles of macroscopic coal samples pyrolyzing and devolatilizing at fire-level radiant flux intensities of 3 to 8 W/cm^2, as reported by Lee, Singer, and Chaiken (*1*).

2. The mass loss rates of pyrolysis and devolatilization of microscopic coal particles as a function of particle size for diameters of 51 to 310 μm, and radiant flux intensities in the range 100 to 400 W/cm^2, reported by Hertzberg and Ng (*12*).

3. Simultaneously obtained SEM photomicrographs of the microscopic morphological structural changes in those particles after their pyrolysis and devolatilization as reported by Hertzberg and Ng (*12*), and as confirmed by new SEM photomicrographs contained in this report.

4. Mass loss rates for the pyrolysis and devolatilization of large samples of PMMA at fire-level radiant fluxes of 1.4 to 4.0 W/cm^2, as reported by Kashiwagi and Ohlemiller (*13*) and Vovelle, Akrich, and Delfau (*27*).

5. Surface temperature measurements made during the above mass loss measurements for PMMA pyrolysis and devolatilization (*13*), as well as similar surface temperature measurements reported by Kashiwagi (*30*).

New data were also presented and analyzed in this report, including

6. Mass loss rates for the pyrolysis and devolatilization of millimeter size diameter rods of PMMA at still higher radiant fluxes of from 12 to 115 W/cm^2.

7. SEM photomicrographs of the microscopic morphological structure of the frozen pyrolysis and devolatilization wave fronts in bituminous and subbituminous coals that were propagation at a flux level of about 115 W/cm^2.

On the basis of this detailed analysis and evaluation, it is concluded that there is no substantive evidence to support the traditional viewpoint that the pyrolysis and devolatilization reaction process occurs isothermally under chemical rate control. There is also no evidence that the process can be described realistically by a classical, unimolecular Arrhenius function of temperature. On the contrary, the overwhelming weight of the available data shows that the reaction process is heat-flux driven and that it proceeds in the form of a highly nonisothermal pyrolysis and devolatilization wave front whose velocity is controlled by the absorbed heat flux intensity relative to the thermodynamic properties of the solid. The structure of that pyrolysis and devolatilization wave front is highly nonisothermal even on the microscopic scale of 50 μm and less. The driving force for the reaction is not the temperature of any one region within that wave front but rather the absorbing heat flux intensity that powers the entire process.

The barrier to the reaction is not some physically obscure Arrhenius, activation energy, nor can the barrier be overcome by considering the temperature in only one region of the system. The real barrier to reaction is the thermal inertia of the entire system, its resistance in the form of the enthalpy required for each element of the solid reactant to reach its decomposition temperature, T_s, plus that required for its devolatilization. That thermal inertia is $\int_{T_o}^{T_s} C(T)\,dT + \Delta H_v$, and its reciprocal is the rate constant for the process. The system can be considered to be under chemical rate control only when the rate of the reaction is near zero; that is, only when the temperature is less than the decomposition temperature. Once the temperature in any region of the system approaches T_s, the rate of the reaction becomes relatively insensitive to that temperature and the process become heat-transport controlled. The temperature of the reactant can approach T_s only if the heat flux exceeds some critical value, and once that happens, the rate is controlled by that flux level.

In such a nonisothermal system of coupled heat and mass transport, the exact temperature of the surface of the phase discontinuity between the products (volatiles) and the reactant (solid) is of secondary importance. While its exact value may not, as yet, have been accurately measured for coal, the available evidence suggests that it remains low and does not vary markedly even as the reaction rate varies by many orders of magnitude. For microscopic coal particles, the generation of a char layer residue masks the reaction zone from the observer, and

makes it very unlikely that the temperature of the reaction zone can be accurately measured by standard optical techniques. The available data suggest that for coal T_s is no higher than 450° to 600° C regardless of the temperature of the heating source. For PMMA, T_s is probably in the range 350° to 550° C.

For Pittsburgh seam bituminous coal the same measured rate constant for pyrolysis and devolatilization can be inferred from either the macroscopic mass loss measurements of Lee, Singer, and Chaiken (*1*), or the microscopic rate measurements of Hertzberg and Ng (*2*). The rate constant is k_t (Pgh coal) = 1.9 mg/cal. Structure data obtained with the SEM show that the intrinsic width of the pyrolysis wave front is the same in both macroscopic and microscopic samples: it is less than 50 μm in width at heating fluxes in the range of 100 W/cm^2 and above.

For PMMA, the rate constant for pyrolysis and devolatilization has been much more accurately measured. The data reported by three independent investigators gives good agreement at

$$k_t(\text{PMMA}) = \left[\int_{T_o}^{T_s} C(T)\, dT + \Delta H_v\right]^{-1} = 0.67 \text{ to } 0.72 \text{ mg/J}.$$

Those measured values are only slightly higher than the predicted value of 0.63 mg/J, which is obtained from the known heat capacities, the heat of depolymerization, and the heat of vaporization of the monomer.

REFERENCES

1. Lee, C. K., J. M. Singer, and R. F. Chaiken. Coal Pyrolysis at Fire-Level Heat Fluxes. Combust. Sci. Technol., v. 16, 1977, pp. 205–213.

2. Hertzberg, M., K. L. Cashdollar, D. L. Ng, and R. S. Conti. Domains of Flammability and Thermal Ignitability for Pulverized Coals and Other Dusts. Paper in the Nineteenth Symposium (International) on Combustion (Haifa, Israel, Aug. 8–13, 1982) Combustion Inst., Pittsburgh, PA, 1982, pp. 1169–1180.

3. Hertzberg, M., I. A. Zlochower, and K. L. Cashdollar. Volatility Model for Coal Dust Flame Propagation and Extinguishment. Paper in the Twenty-first Symposium (International) on Combustion (Munich, Federal Republic of Germany, Aug. 3–8, 1986). Combustion Inst., Pittsburgh, PA, 1987.

4. Alameddin, A. N., and S. J. Luzik. Coal Dust Explosions in the Cement Industry. Paper in Industrial Dust Explosions, ASTM STP 958. American Society for Testing and Materials, Philadelphia, PA, 1987 pp. 217–233.

5. Zalosh, R. G. Review of Coal Pulverizer Fire and Explosion Incidents. Paper in Industrial Dust Explosions, ASTM STP 958. American Society for Testing and Materials, Philadelphia, PA, 1987, pp. 191–201.

6. Carini, R. C., and K. R. Hules. Coal Pulverizer Explosions. Paper in Industrial Dust Explosions, ASTM STP 958. American Society for Testing and Materials, Philadelphia, PA, 1987, pp. 202–216.

7. Conti, R. S., and M. Hertzberg. Thermal Autoignition Temperatures From the 1.2-L Furnace and Their Use in Evaluating the Explosion Potential of Dusts. Paper in Industrial Dust Explosions, ASTM STP 958. American Society for Testing and Materials, Philadelphia, PA, 1987, pp. 45–59.

8. Van Krevelen, D. W. Coal Typology-Chemistry-Physics-Constitution. Elsevier, 1961, 514 pp.

9. Badzioch, S., and P. G. W. Hawksley. Kinetics of Thermal Decomposition of Pulverized Coal Particles. Ind. Eng. Chem. Process Des. Dev., v. 9, 1970, pp. 521–530.

10. Howard, J. B. Fundamentals of Coal Pyrolysis and Hydropyrolysis. Ch. 12 in Chemistry of Coal Utilization, Second Supplementary Volume, ed. by M. A. Elliott. Wiley, 1981, pp. 665–784.

11. Ng, D. L., M. Hertzberg, and J. C. Edwards. A Microscopic and Kinetic Study of Coal Particle Devolatilization in a Laser Beam. Poster Session Paper No. 83, pres. at The Twentieth Symposium (International) on Combustion (Ann Arbor, MI, Aug. 12–17, 1984). Combustion Inst., Pittsburgh, PA, 1984, p. 189.

12. Hertzberg, M., and D. L. Ng. A Microscopic and Kinetic Study of Coal Particle Devolatilization in a Laser Beam. Paper in Fundamentals of Physical-Chemistry of Pulverized Coal Combustion, ed. by J. Lahaye and G. Prado, NATO ASI Series E, No. 137, Martinus Mijhoff, 1987, pp. 104–125.

13. Kashiwagi, T., and T. J. Ohlemiller. A Study of Oxygen Effects on Nonflaming Transient Gasification of PMMA and PE During Thermal Irradiation. Paper in the Nineteenth Symposium (International) on Combustion (Haifa, Israel, Aug. 8–13, 1982). Combustion Inst., Pittsburgh, PA, 1982, pp. 815–823.

14. Niksa, S., L. E. Heyd, N. B. Russel, and D. A. Saville. On the Role of Heating Rate in Rapid Coal Devolatilization. Paper in the Twentieth Symposium (International) on Combustion (Ann Arbor, MI, Aug. 12–17, 1984). Combustion Inst., Pittsburgh, PA, 1984, pp. 1445–1453.

15. Chermin, H., A. G., and D. W. Van Krevelen. Chemical Structure and Properties of Coal—A Mathematical Model of Coal Pyrolysis. Fuel, v. 36, 1957, pp. 85–104.

16. Juntgen, H., and K. H. van Heek. Gas Release From Coal as a Function of the Rate of Heating. Fuel, v. 47, 1968, pp. 103–117.

17. Kobayashi, H. Devolatilization of Pulverized Coal at High Temperatures. Ph. D. Thesis, MA Inst. Technol., Cambridge, MA, 1976, pp. 280–284.

18. Zielinski, E. The Evolution of Volatile Matter From Pulverized Coal Particles. Fuel, v. 46, 1967, pp. 329–340.

19. Serio, M. A., P. R. Solomon, D. G. Hamblen, J. R. Markham, and R. A. Carangelo. Coal Pyrolysis Kinetics and Heat Transfer in Three Reactors. Poster Session Paper No. 76, pres. at the Twenty-first Symposium (International) on Combustion (Munich, Federal Republic of Germany, Aug. 3–8, 1986). Combustion Inst., Pittsburgh, PA, 1986, p. 158.

20. Freihaut, J. D., and F. J. Vastola. A Computational Examination of the Effect of Coupled Heat Transport and Chemical Kinetics Upon Single Particle Coal Pyrolysis. Eastern Section of the Combustion Institute, Fall Technical Meeting (Miami Beach, FL, Nov. 29–Dec. 1, 1978). Combustion Inst., Pittsburgh, PA, 1978, pp. 32-1—32-4.

21. Solomon, P. R., and M. A. Serio, Evaluation of Coal Pyrolysis Kinetics. Paper in Fundamentals of Physical Chemistry of Pulverized Coal Combustion, ed. by J. Lahaye and G. Prado. NATO ASI Series E, No. 137, Martinus Mijhoff, 1987, pp. 126–151.

22. Merrick, D. Mathematical Models of the Thermal Decomposition of Coal. 1. The Evolution of Volatile Matter. Fuel, v. 62, 1983, pp. 534–570.

23. Solomon, P. R., R. M. Corangelo, P. E. Best, J. R. Markham, and D. G. Hamblen. The Spectral Emittance of Pulverized Coal and Char. Paper in the Twenty-first Symposium (International) on Combustion (Munich, Federal Republic of Germany, Aug. 3–8, 1986). Combustion Inst., Pittsburgh, PA, in press.

24. Hertzberg, M. The Free Laminar and the Laser-Induced Combustion of Ammonium Perchlorate. Combust. Sci. and Technol., v. 1, 1970, pp. 449–460.

25. Hertzberg, M. The Combustion of Pure and Composite Propellants. The Expansion and Application of Laminar Flame Theory To Heterogeneous Solid Propellants. Oxid. Combust. Rev., v. 5, 1971, pp. 1–81.

26. Pellett, G. Ammonium Perchlorate Gasification and Combustion at High Heating Rates and Low Pressures. Paper in The Fourteenth Symposium (International) on Combustion (University Park, PA, Aug. 20–25, 1972), Combustion Inst., Pittsburgh, PA, 1973, pp. 1317–1330, and comment by M. Hertzberg, pp. 1328–1329.

27. Vovelle, C., R. Akrich, and J. L. Delfau. Mass Loss Rate Measurements on Solid Materials Under Radiative Heating. Combust. Sci. Technol., v. 36, 1984, pp. 1–18.

28. Bares, V., and B. Wunderlich. Heat Capacity of Molten Polymers. J. Polym. Sci., Polym. Phys. Ed., v. 11, 1973, pp. 861–872.

29. Irvin, K. J. Heat and Entropies of Polymerization. Polymer Handbook, ed. by J. Brandup, and E. H. Immergut. Wiley, 2d ed., 1975, pp. II–425 and V–56.

30. Kashiwagi, T. Experimental Observation of Radiative Ignition Mechanisms. Combust. Flame, v. 34, 1979, pp. 231–244.

31. Stull, D. R., E. F. Westrum, Jr., and G. C. Sinke. The Chemical Thermodynamics of Organic Compounds. Wiley, 1969, 865 pp.

32. Ng, D. L., K. L. Cashdollar, M. Hertzberg, and C. P. Lazzara. Electron Microscopy Studies of Explosion and Fire Residues. BuMines IC 8936, 1983, 63 pp.

33. Zien, T. F. Integral Solutions of Ablation Problems With Time-Dependent Heat Flux. AIAA J., v. 16, No. 12, Dec. 1978, pp. 1287–1295.

34. Carslaw, H. S., and J. C. Jaeger. Conduction of Heat in Solids, Oxford-Clarendon Press, 2d ed., 1959, p. 75.

35. Ames, W. F. Numerical Methods for Partial Differential Equations. Barnes and Noble, Inc., New York, 1969, p. 52.

36. Chaiken, R. F., W. H. Andersen, M. K. Barsh, E. Mishuck, G. Moe, and R. D. Schultz. Kinetics of Surface Degradation of Polymethylmethacrylate. J. Chem. Phys., v. 32, 1960, pp. 141–146.

37. Barsh, M. K., W. H. Andersen, K. W. Billo, G. Moe, and R. D. Schultz. Improved Instrument for the Measurement of Linear Pyrolysis Rates of Solids. Rev. Sci. Instr., v. 29, 1958, pp. 392–395.

38. Landau, L. D., and E. M. Lifshitz. Fluid Mechanics. Pergamon (New York), 1959, p. 347.

APPENDIX A.—SYMBOLS AND NOMENCLATURE

A_p	particle area
α	proportionality constant
β	proportionality constant
a_o	edge length of cubic particle
C(T)	heat capacity
d	characteristic sample diameter
$\overline{D}_s$ or D_p	particle diameter
δ	characteristic penetration depth of the pyrolysis and devolatilization wave front, or depth of the subsurface temperature profile
$\frac{dm(t)}{dt}$	time rate of change of mass of reactant
$\frac{\partial T}{\partial t}$	time derivative of temperature
$\frac{\partial T}{\partial x}$	spatial derivative of temperature
ΔH_v	heat of vaporization or devolatilization
Δm	area weight loss; that is, mass loss per unit cross-sectional area of sample
$\Delta\rho$	density difference between hot and cold gas in a natural convective flow
E_a	activation energy
ϵ_p	particle emissivity
g	gravitational acceleration
I	radiant heat source flux intensity
I_ℓ	net loss flux
I_ℓ'	sum of reflectance loss and net loss flux
k	reaction rate constant
k′	proportionality rate constant
k_o	preexponential factor
k_t	rate coefficient or constant for the pyrolysis and devolatilization process under heat transport control
λ	thermal conductivity
$m(\infty)$	final mass of reactant as $t \rightarrow \infty$
m_o	initial mass of reactant at $t = 0$
$\dot{m}$	mass loss rate per unit area
m(t)	mass of reactant after an exposure time, t
Nu	Nusselt number
r	surface reflectance
R	universal gas constant
rI	reflectance loss flux
ρ	mass density
σ	Stefan-Boltzmann constant
t	time
$t_{1/2}$	devolatilization half-life for a particle
t_{dv}	particle devolatilization time
T	temperature or the particle temperature
T_c	maximum char temperature
T_h	source temperature to which a particle is exposed
T_o	initial temperature
T_s	decomposition temperature or surface temperature, or temperature of the zone of active pyrolysis and devolatilization
T(x,t)	temperature as a function of the linear coordinate and time
v_b	buoyant velocity in convective flows
τ	induction time
V_p	particle volume
V(t)	volatile yield after an exposure time, t
$V(\infty)$	maximum volatile yield as $t \rightarrow \infty$
x	a linear coordinate
$\dot{x}_o$	surface regression rate during pyrolysis and devolatilization

APPENDIX B.—ANALYSIS OF HOTPLATE PYROLYSIS DATA FOR PMMA

Laser pyrolysis data for polymethylmethacrylate (PMMA) were presented in figures 12 and 13 of the main text and they compared quite favorably with the data of other researchers (*13, 27, 30*)[1] obtained at lower radiant fluxes (figs. 9–11). The literature, however, also contains even earlier data that were reported by Chaiken (*36*) using a hotplate pyrolysis technique (*37*). In that technique, the PMMA sample was pressed against an electrically heated hotplate whose temperature was maintained at some constant source temperature, T_h. At low contact pressures, the measured rates were somewhat sensitive to the contact pressure between the hotplate and the PMMA sample because of the necessity of maintaining good thermal contact between the sample and the heat source (*37*). At higher contact pressures, the results were complicated by "thermal and mechanical deformation of the material being tested." But there was a range of contact pressures in which good thermal contact was obtained, and the measured pyrolysis rates were pressure independent. For PMMA, that range of contact pressures was about 0.6 to 1.0 atm, and pyrolysis rate data were reported for contact pressures in that range (*37*). For hotplate source temperatures, T_h, in the range of 400° to 700° C, their linear pyrolysis rates for low density (non-crosslinked) PMMA varied in the range between $\dot{x}_o$ = 0.007 cm/s and $\dot{x}_o$ = 0.09 cm/s (*36*). Those linear rates of pyrolysis and devolatilization correspond to mass loss flux values, $\dot{m}$, in the range of 8 to 106 mg/(cm^2·s). Those measured mass fluxes for hotplate pyrolysis are in the same range as the data reported here at high laser flux intensities (fig. 13). Chaiken also collected and analyzed the pyrolysis gases, and their chemical analysis confirmed that the product gas consisted almost entirely of the mononomer, methylmethacrylate.

Those hotplate pyrolysis measurements were analyzed by Chaiken according to the traditional mechanism, and under the traditional assumption that $T_h = T_s$. As shown earlier, that assumption is generally not justified. Accordingly, it is important to reanalyze the data in terms of the flux-driven, heat-transport-limited model presented here. Chaiken's PMMA data are summarized in the first three columns of table B–1. The hotplate source temperatures are shown in column 1, and the measured $\dot{x}_o$ values at each temperature are shown in column 2. The mass loss fluxes, $\dot{m} = \rho\dot{x}_o$, corresponding to those linear pyrolysis rates are shown in column 3. Those $\dot{m}$ values are then transformed into equivalent net input heating fluxes, I_{net}, using the laser pyrolysis data reported in figure 13. Those equivalent net heating fluxes are shown in column 4, and they represent the net fluxes required to maintain their measured pyrolysis rates for each hotplate temperature exposure.

Now the net heating flux into the surface of a pyrolyzing and devolatilizing solid (or liquid) whose surface temperature is at T_s while it is in contact with a hotplate at the temperature, T_h, is given by the sum of the conductive flux, I_c, and the radiant flux, I_r. Thus

$$I_{net} = I_c + I_r = \lambda_g\left(\frac{dT}{dx}\right)_s + \epsilon_h\sigma T_h^4 - \epsilon_s\sigma T_s^4, \quad \text{(B–1)}$$

where $\left(\frac{dT}{dx}\right)_s$ is the temperature gradient into the surface of the PMMA sample from the pyrolysis volatiles above the surface that are in thermal contact with the hotplate. The thermal conductivity of those gas volatiles is λ_g. The quantities ϵ_h and ϵ_s are the emissivities of the hotplate and the sample respectively, and σ is the Stefan-Boltzmann constant. Calculated radiant fluxes are shown in column 5 and they were obtained under the assumption of unit emissivities for both surfaces. Clearly the radiant flux contribution from the hotplate at those temperatures is trivial in comparison to the net flux required to sustain their measured pyrolysis rates.

The major flux input driving the pyrolysis wave is thus clearly the conductive flux, I_c, whose magnitude is shown in column 6. That conductive flux across the pyrolysis gas interface between the hotplate source at T_h and the PMMA surface at T_s is proportional to the temperature gradient, which is approximated as

$$\left(\frac{dT}{dx}\right)_s = \frac{T_h - T_s}{\delta_g}, \quad \text{(B–2)}$$

where δ_g is the separation distance between the hotplate and the pyrolyzing and devolatilizing PMMA surface. Combining equations B–1 and B–2 and solving for the separation distance gives

$$\delta_g = \frac{\lambda_g (T_h - T_s)}{I_c}. \quad \text{(B–3)}$$

In the traditional analysis it is assumed that $T_h = T_s$ and that $\delta_g = 0$. As shown earlier, such an assumption is unrealistic. It is as unrealistic for the hotplate source as it is for the drop furnace, the electrically heated screen, or the laminar flow flame. As discussed earlier, an isothermal condition between the hotplate source of heat and the vaporizing heat sink at the surface would mean that the heat flux into the surface was zero. In the absence of such a heat flux to sustain the endothermic vaporization process, there could be no pyrolysis and devolatilization. For the hotplate system the traditional assumption that $T_h = T_s$ and that $\delta_g = 0$, also violates the mass conservation requirements. The quantity δ_g is not simply the gap separation distance between the two surfaces in contact, it is also the essential channel through which pyrolysis gases must flow as the PMMA devolatilizes. Thus the traditional assumptions that $\delta_g = 0$ and $T_h = T_s$ violate both the energy and the mass transport requirements for the system being studied. Accordingly, those assumptions are rejected, and in the analysis being presented here, the quantities T_s and δ_g are treated as unknowns whose values are to be determined from the data summarized in columns 1 through 6 of table B–1.

[1] Italic numbers in parentheses refer to items in the list of references preceding appendix A.

Table B–1.—Analysis of hotplate pyrolysis data for PMMA

(1)	(2)	(3)	(4)	(5)	(6)	(7)	(8)	(9)	(10)
T_h, °C	$\dot{x}_o$, cm/s	$\dot{m}$, mg/(cm²·s)	I_{net}, W/cm²	I_r, W/cm²	I_c, W/cm²	$\rho_g c_o$, g/(cm²·s)	δ_g, μm	λ_g, mW/(cm·K)	T_s, °C
700	0.090	106	147	4	143	39.0	6	0.72	581
600	.049	58	81	2	79	40.5	3	.64	563
529	.028	33	46	1.0	45	41.8	2	.58	513
500	.021	25	35	.8	34	42.6	1	.56	494
400	.007	8	8	.3	8	46.0	.4	.47	398

One can determine the absolute magnitude of δ_g from the mass flow conservation constraint. The mass flow of monomer gas from the devolatilizing surface is $\dot{M} = \dot{m}\,\ell_o^2$, where ℓ_o is the edge width of the square cross section of the PMMA strand, which was 0.6 cm. The monomer gas flows rapidly outward between the two surfaces through the channel formed by the separation distance, δ_g. Gas exits from that channel through its periphery, flowing through an area $A = 4\,\ell_o\,\delta_g$. The exiting mass flow is $\dot{M} = \rho_g\,v_g\,A = 4\,\ell_o\,\delta_g\,\rho_g\,M_a\,c_o$, where ρ_g is the gas density at the exit, v_g is the gas velocity, M_a is the flow mach number, and c_o is the local sound velocity. Equating source mass flow from the pyrolyzing surface with exit mass flow from edges of the separation gap, and solving for required separation distance gives:

$$\delta_g = \frac{\dot{m}\,\ell_o}{4\,\rho_g\,c_o\,M_a} \quad . \tag{B–4}$$

One assumes that the contact pressure between hotplate and vaporizing PMMA surface was maintained at a sufficiently high level to insure that the flow within the channel was sonic. For choked flow conditions for the monomer, whose ratio of specific heats is $\Upsilon = 1.1$, the maximum flow mach number is $M_a = 0.60$ (*38*). The appropriate $\rho_g\,c_o$ values at each temperature are shown in column 7 of table B–1. Equation B–4 is then used to calculate the gap separation distances that are tabulated in column 8.

Clearly, according to this reanalysis, it is that finite separation distance that corresponds to the condition of good thermal contact, rather than the condition of $\delta_g = 0$, which is assumed in the traditional analysis. Actually, an adequate explanation of the full range of results obtained in the hotplate pyrolysis experiments, especially the contact pressure dependence of the rate, requires that δ_g be considered as finite (*37*). At low contact pressures between the hotplate and the pyrolyzing surface, i.e., below 0.6 atm, the measured $\dot{m}$ values were pressure dependent, increasing with increasing contact pressure. Those results were explained as being due to poor thermal contact between the two surface, which, of course, is equivalent to saying that δ_g was larger than its minimum possible value. An increase in the contact pressure naturally causes δ_g to decrease, which increases the conductive flux, which increases the rate of devolatilization. In the contact pressure range between 0.6 and 1.0 atm, the $\dot{m}$ values were pressure insensitive, and that was interpreted to mean that there was good thermal contact, which, according to the traditional assumption was taken to mean that $\delta_g = 0$. In this reanalysis, it is equation B–4 that serves as the quantitative means of defining the degree of thermal contact between the two surfaces that is necessary to maintain the required conductive heat flux. Clearly good thermal contact occurs at a minimum, but finite average value of δ_g, in the range of 0.4 to 6 μm. Such a finite value is here given by the value required to satisfy mass transport constraints.

The final step in this reanalysis is to solve equation B–3 for the surface temperature, T_s:

$$T_s = T_h - I_c\,\delta_g/\lambda_g, \tag{B–5}$$

and to substitute the δ_g values in column 8 and the I_c values in column 6 into equation B–5. With those substitutions, and using the thermal conductivity (λ_g) values listed in column 9, one can calculate the surface temperature, T_s. Those values are listed in column 10.

As can be seen, for the highest devolatilization rate at a hotplate temperature of 700° C, the reactant temperature, T_s, is 119° C colder than the source temperature, T_h. For the lowest rate shown, the PMMA surface is only about 2° C colder. While these corrections are relatively modest for this PMMA case, in other cases the required corrections are very large. For example, for coal particles devolatilizing in drop furnaces or laminar flow reactors, the δ_g values are orders of magnitude larger than the highest value listed in table B–1. Conductive heat transfer from the high-temperature gas at T_h to the initially cold particle involves a boundary layer thickness, δ_g, that is at least equal to the diameter of the particle, which is typically about 40 μm. For comparable I_{abs} requirements, the temperature difference $T_h - T_s$ will, according to equation B–5, be an order of magnitude higher. In addition to that normal boundary layer thickness, as the particle heats to T_s, the volatiles emitting from the surface during devolatilization are much cooler than T_h, and their outward flow causes a marked increase in the boundary layer thickness. Accordingly, for coal particles at comparable mass loss rates to those shown in table B–1, the temperature difference $T_h - T_s$ will be at least an order of magnitude higher than the values calculated for PMMA.

U.S. GOVERNMENT PRINTING OFFICE: 1988 — 547-000/80,035

INT.-BU.OF MINES,PGH.,PA. 28714